THE GEOLOGICAL SOCIETY OF AMERICA®

Late Quaternary climatic controls on erosion rates and geomorphic processes in western Oregon, USA

Jill A. Marshall[1,†], Joshua J. Roering[1], Daniel G. Gavin[2], and Darryl E. Granger[3]
[1]*Department of Earth Sciences, 1272 University of Oregon, Eugene, Oregon 97403, USA*
[2]*Department of Geography, 1251 University of Oregon, Eugene, Oregon 97403, USA*
[3]*Department of Earth, Atmospheric, and Planetary Sciences, Purdue University, 550 Stadium Mall Drive, West Lafayette, Indiana 47907, USA*

ABSTRACT

Climate regulation of erosion in unglaciated landscapes remains difficult to decipher. While climate may disrupt process feedbacks that would otherwise steer landscapes toward steady erosion, sediment transport processes tend to erase past climate landforms and thus bias landscape evolution interpretations. Here, we couple a 50 k.y. paleoenvironmental record with 24 ^{10}Be-derived paleo-erosion rates from a 63-m-thick sediment archive in the unglaciated soil-mantled Oregon Coast Range. Our results span the forested marine oxygen isotope stage (MIS) 3 (50–29 ka), the subalpine MIS 2 (29–14 ka), and the forested MIS 1 (14 ka to present). From 46 ka through 28.5 ka, erosion rates increased from 0.06 mm yr^{-1} to 0.23 mm yr^{-1}, coincident with declining temperatures. Mean MIS 2 erosion rates remained at 0.21 mm yr^{-1} and declined with increasing MIS 1 temperatures to the modern mean rate of 0.08 mm yr^{-1}. Paleoclimate reconstructions and a frost-weathering model suggest periglacial processes were vigorous between 35 and 17 ka. While steady erosion is often assumed, our results suggest that climate strongly modulates soil production and transport on glacial-interglacial time scales. By applying a cosmogenic paleo-erosion model to evaluate ^{10}Be concentrations in our sedimentary archive, we demonstrate that the depth of soil mixing (which is climate-dependent) controls the lag time required for cosmogenic erosion rates to track actual values. Our results challenge the widely held assumption that climate has minimal impact on erosion rates in unglaciated midlatitude terrain, which invites reconsideration of the extent to which past climate regimes manifest in modern landscapes.

INTRODUCTION

In unglaciated settings ranging from temperate to tropical, we are currently unable to accurately predict if climate change over glacial-interglacial intervals will increase or decrease erosion. As a result, the extent to which climate modulates landscape dynamics, such as river incision or aggradation, and invokes process thresholds that may promote new equilibrium states remains unresolved (Chorley et al., 1984; Tucker and Slingerland, 1997). Under steady uplift, geomorphic process feedbacks steer landscapes toward a dynamic equilibrium, such that erosion balances uplift over long time scales (Ahnert, 1994; Hack, 1975). However, it remains unclear how variations in precipitation or temperature patterns in unglaciated terrain disrupt landscape adjustment (Chorley et al., 1984) and produce transient signatures.

The onset of increased climatic variability during the Pleistocene (Molnar, 2004) may have increased the frequency of landscape process perturbations such that repeated departures from steady-state adjustment led to accelerated sedimentation rates starting 4–2 Ma (Zhang et al., 2001). However, a preservation bias in the sediment accumulation record skewed toward younger deposits may negate this interpretation (Sadler, 1981; Schumer and Jerolmack, 2009; Willenbring and Jerolmack, 2015). While a global analysis of 18,000 bedrock thermochronometric ages from mountainous regions suggests erosion rates have increased rapidly since ca. 2 Ma, even in unglaciated terrain (Herman et al., 2013), the extent to which this analysis is biased due to precision limits inherent to the thermochronologic method remains unresolved (Willenbring and Jerolmack, 2015). Further, these global-scale analyses have limited ability to infer process controls on climate-erosion linkages, which is paramount for establishing robust and testable models of landscape dynamics. Without a mechanistic framework for the way in which climate controls processes and rates, it is difficult to parse how climate-driven changes in hillslope or fluvial processes influence landscape evolution.

The onset of glaciation is viewed as an "abrupt and radical change" in a landscape's erosional environment and history (Church and Ryder, 1972, p. 3059), with morphologic, modeling, and cosmogenic studies quantifying landscape response in terms of wider and deeper valleys, greater relief, and rapid denudation (Brocklehurst and Whipple, 2002; Herman and Braun, 2008; Montgomery, 2002). Despite recent advances, the legacy of past climates in unglaciated, soil-mantled settings is still difficult to discern, as topographic evidence such as solifluction lobes are likely turbated by biota over millennia and shielded from view in forested settings. Additionally, in tectonically active areas, soil residence times are short; modern processes quickly erase past signals, and sediment archives are rare.

Our knowledge gap regarding the legacy of past climates in unglaciated terrain hampers progress in a broad array of problems in geomorphology and critical zone science, such as: quantifying fluxes of sediments and solutes, modeling landscape response to past and present climate change, and estimating the regulation of global CO_2 by silicate weathering (Anderson et al., 2013; Dietrich and Perron, 2006; Dietrich et al., 2003; National Research Council, 2010).

Cosmogenic nuclides, with applicability over time scales of 10^3 to 10^5 yr, overlap with the time scales over which rocks weather, soils form, climates cycle between glacial and interglacial, and rivers incise or aggrade (Granger and Schaller, 2014). To better understand how variations in temperature or precipitation may control landscape response, one approach is to quantify changes in sediment production or erosion rates across a suite of study sites with similar lithology and tectonics but differences in precipitation or temperature regimes. In a set

†Present address: Department of Earth and Planetary Science, University of California–Berkeley, 307 McCone Hall, Berkeley, California 94720, USA; jmarshall@berkeley.edu.

 doi: 10.1130/B31509.1; 9 figures; 3 tables; Data Repository item 2016362.

of seminal studies, Riebe et al. (2001a, 2001b) found little correlation between temperature or precipitation and cosmogenic radionuclide (CRN)–derived erosion rates across the Californian Sierran granites. It is challenging to compare sites with different climate regimes, because landscapes are likely to be polygenetic, with modern processes acting on terrain shaped by past tectonics, climates, weathering regimes, hydrologic routing patterns, and states of landscape adjustment (Barry, 1998; Bull, 1991; Chorley et al., 1984; Slim et al., 2015). Thus, space for time substitutions may preclude comparisons of climatic control on erosion rates, as climate may not be the only controlling variable (Pederson et al., 2001).

Alternatively, "drilling" through time at a single location with steady tectonic forcing allows for the evaluation of climate controls on erosion rates and mechanisms. Empowered by technological advances such as CRN and luminescence dating, recent studies have deduced changes in erosion rates related to changes in rainfall in unglaciated areas, including Oman (Blechschmidt et al., 2009), central Peru (Bekaddour et al., 2014; McPhillips et al., 2013), and Texas, United States (Hidy et al., 2014). Over longer time scales, Charreau et al. (2011) observed potential evidence for rapid erosion in the Tian Shan with the onset of the Quaternary ice ages, while Refsnider (2010) quantified a nearly order-of-magnitude increase in erosion rates in unglaciated Rocky Mountain terrain between 4.9 and 1.2 Ma, attributed to mid-Pleistocene climate-driven periglacial processes. These studies have yielded excellent data sets for future testing with process-based models.

Other CRN-derived paleo-erosion rates suggest enhanced periglacial erosion during the Pleistocene compared to modern temperate climate erosion rates. In the unglaciated Garhwal Himalaya, Pleistocene erosion rates were ~2–4× greater than modern and have been attributed to either enhanced periglacial sediment production or a modern reduction in landsliding due to slope readjustment (Scherler et al., 2015). In unglaciated central Europe, CRN-derived erosion rates during the Pleistocene were ~3× faster than modern values and have been attributed to vigorous periglacial processes (Schaller et al., 2002). Similarly, in the unglaciated Oregon Coast Range, ^{10}Be-derived erosion rates were ~2.5× greater during the Last Glacial Maximum (LGM) than modern rates, and this change has been attributed to LGM frost processes based on paleoclimate reconstructions and simulations combined with a frost-cracking model (Marshall et al., 2015). These interpretations are supported by studies in the French Alps, where CRN-derived erosion rates increase with increasing elevation, covarying with temperature and the relative intensity of frost weathering (Delunel et al., 2010), suggesting a mechanistic link between temperature and bedrock erosion (Hales and Roering, 2007; Walder and Hallet, 1985).

Recent paleo-erosion climate studies, while advancing our quantitative knowledge of linkages between climate and erosion rates, are often limited by short temporal spans or coarse resolution or cover too diverse an area to allow for definitive process interpretations. Quiescent settings such as lake deposits have the highest probability of recording periodic fluctuations in climatic signals and, in regions of steady uplift, avoid problematic polygenesis. An ideal paleosetting would span more than one climatic interval (e.g., marine oxygen isotope stage [MIS]), in a single quartz-rich lithology (for CRN-derived erosion rates), with direct hillslope-to-basin deposition, and contain abundant proxy data such as fossils for inferring millennial-scale climate variations (Jerolmack and Paola, 2010; Niemi et al., 2005; Schaller and Ehlers, 2006; Schumer et al., 2011; von Blanckenburg, 2005).

Little Lake, a remnant of a much larger paleolake in the Pacific Northwest Oregon Coast Range (OCR) that has been well studied by paleoecologists, provides a near-ideal setting for quantifying climate-induced erosion rates through time (Fig. 1). By combining a high-fidelity 50 k.y. record of ^{10}Be-derived erosion rates, sediment stratigraphy, and vegetation-derived climate data extracted from a new Little Lake sediment core, we infer millennial-scale changes in climate, surface processes, and erosion rates. The sedimentary core data span the preglacial MIS 3 (50–29 ka), the glacial MIS 2 (29–14 ka), and the modern interglacial MIS 1 (13 ka to present) intervals (Lisiecki and Raymo, 2005).

Next, we first provide a geologic and geomorphic overview of the well-studied Oregon Coast Range and describe the Little Lake setting. We then provide a brief background on the use of cosmogenic nuclides and the assumption of steady-state denudation applied to landscapes with variable erosion rates. Because variable soil mixing depths and soil production rates (due to climate-driven ecosystem and process changes) can influence apparent (measured) erosion rates estimated via cosmogenic nuclides, we present a soil production–driven nuclide concentration model to consider transient erosion rates. This conceptual model motivates our preliminary Little Lake erosion rate simulations, allowing us to estimate actual erosion rates using temporal variations in ^{10}Be concentrations from our sediment core.

GEOGRAPHIC SETTING AND PREVIOUS STUDIES

Oregon Coast Range

The well-studied, unglaciated, soil-mantled OCR is a steep and highly dissected mountainous landscape with relatively uniform ridge and valley form (Dietrich and Dunne, 1978; Reneau and Dietrich, 1991). OCR precipitation averages 1–2 m annually, with wet rain-dominated winters, and occasional patchy snow at higher elevations. The summers are generally dry, and mean annual temperatures average ~11 ± 1 °C (mean ± standard error [SE]; PRISM Climate Group, 2010), The wet, temperate climate supports a closed-canopy forest dominated by Douglas fir (*Pseudotsuga menziesii*) and western hemlock (*Tsuga heterophylla*). The underlying sandstone, primarily the Eocene Tyee Formation, is a quartz-rich sequence of uniform, little-deformed, rhythmically bedded turbidite sequences overlying accreted volcanic basement (Heller and Dickinson, 1985; Orr et al., 1992). Tree-driven bedrock to soil conversion dominates modern weathering processes in the OCR (Anderson et al., 2002; Heimsath et al., 2001; Roering et al., 2010). Soils are generally thin on noses and side slopes, with average depths of <0.5 m (Heimsath et al., 2001; Reneau and Dietrich, 1991; Roering et al., 2010). Soils are thicker (~1 m) in unchanneled hollows and provide source material for shallow landslides that can initiate valley-carving debris flows (Dietrich and Dunne, 1978; Stock and Dietrich, 2006).

The OCR is often considered an ideal representation of steady-state topography (Montgomery, 2001; Reneau and Dietrich, 1991; Roering et al., 1999, 2001, 2007), as numerous studies suggest that millennial-scale erosion rates (e.g., Balco et al., 2013; Bierman et al., 2001; Heimsath et al., 2001) balance rock uplift (Kelsey et al., 1996). Long-term uplift rates in the OCR are from 0.05 to 0.3 mm yr^{-1}, with much of the variation in uplift rates due to structural controls along the coast (Kelsey et al., 1996). Modern CRN-derived erosion rates from stream sediments range from ~0.05 to 0.14 mm yr^{1} (Balco et al., 2013; Bierman et al., 2001; Heimsath et al., 2001). (We have adjusted previously reported values to account for muon production in rapidly eroding settings.) Short-term (e.g., decadal to centennial) or localized erosional variability is a reflection of stochastic processes (Heimsath et al., 2001; Sweeney et al., 2012) and rock properties (Marshall and Roering, 2014).

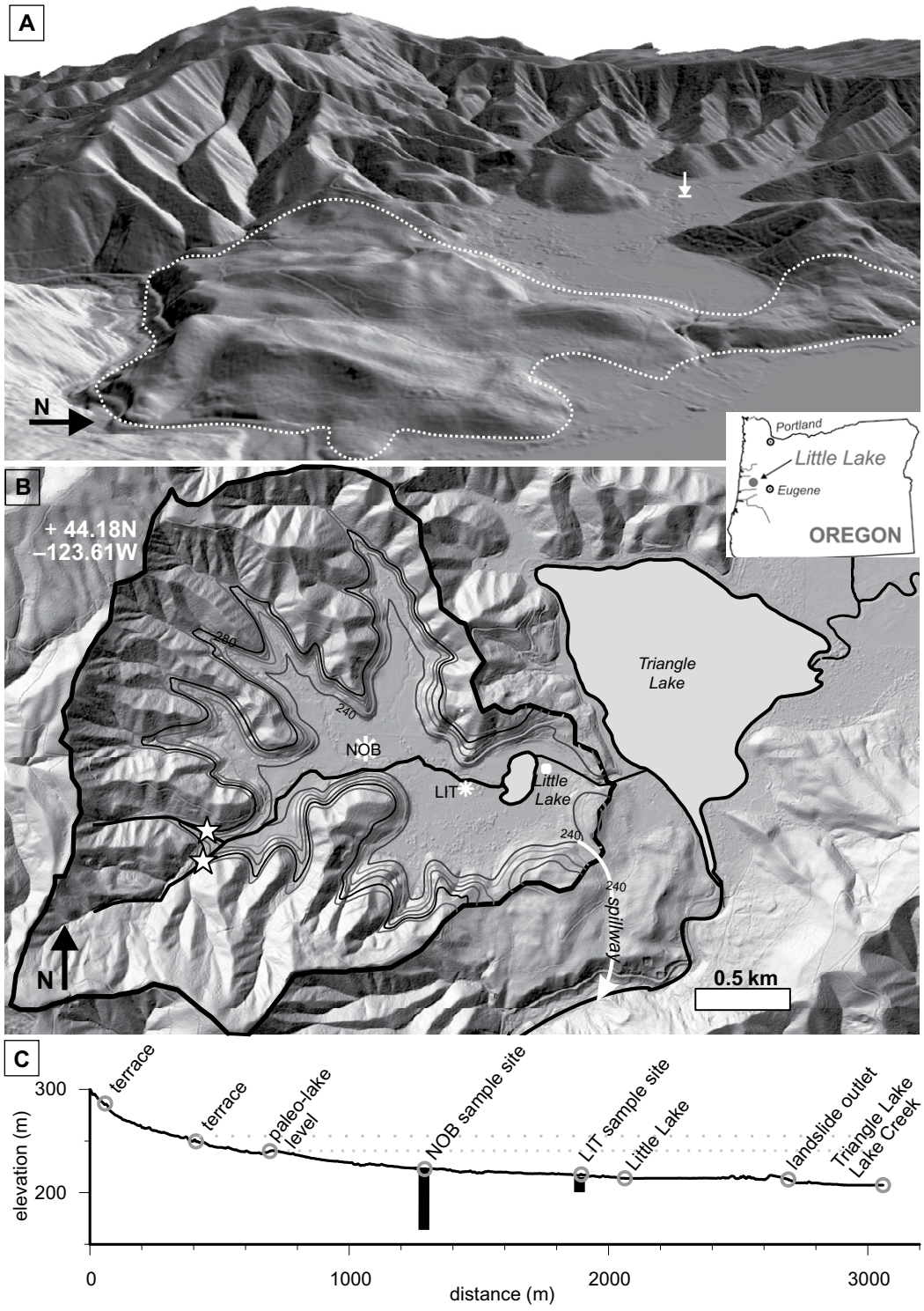

Figure 1. Little Lake catchment and sample sites. (A) Perspective view of the Little Lake basin with landslide deposits and Triangle Lake in the foreground. View is rotated with north to the right. The white arrow delineates the NOB sampling site, and the white dotted line outlines the landslide deposit. (B) Map of the Little Lake catchment and sample sites. Modern stream sample locations are marked with stars. Core data locations are marked with asterisks (labeled NOB, LIT). Previous paleoecology data collected in the fens near the Little Lake outlet are marked with a polygon. Map shows only a portion of the larger landslide-dammed paleolake deposit, which extends to the east of modern Triangle Lake. Contour lines on the map are at 10 m intervals and highlight bench-cut terraces and the abandoned spillway. (C) Longitudinal transect from catchment above NOB sample site to lake outlet. Dashed lines indicate paleo-–water levels inferred from terrace elevations.

Little Lake Basin Physiography

The ~6 km^2 Little Lake catchment, located in the central portion of the OCR (Fig. 1), is composed of steep, highly dissected hillslopes. Little Lake, along with the adjoining Triangle Lake, formed ca. 50 ka (see Results—Chronology section) as the result of a structurally controlled deep-seated landslide. The landslide dam separates present-day Little Lake from Triangle Lake, though the beveled dam deposit and terrace levels on adjoining hillslopes suggest that Little Lake and Triangle Lake may have been part of a single paleolake in the past (Fig. 1A). The areal extent of the Little Lake valley floor is ~1 km^2, and the sedimentary deposit impounded upstream of the landslide dam is over 60 m thick (Oregon Water Resource Department, 2014).

The Little Lake basin attributes make it an ideal location in which to test hypotheses on linkages between climate-driven ecosystem changes and millennial-scale variations in erosion rates. The OCR remained unglaciated during MIS 2, when the Cordilleran ice sheet extended ~400 km to the north of Little Lake. Sediments derived from colluvial processes are the primary source of basin deposits in Little Lake, owing to the lack of deep-seated landsliding within the source catchment. As the basin is underlain by uniform, quartz-rich sandstone (Chan and Dott, 1986; Lovell, 1969; Snavely et al., 1964), it is ideally suited for deriving cosmogenic nuclide erosion rates from quartz grains. Additionally, the paleoenvironmental reconstructions allow us to consider how climate change manifests as changes in soil production and erosion mechanisms.

Light detection and ranging (LiDAR) data, acquired by the National Center for Airborne Laser Mapping, illuminates the landslide deposit that impounded the river as well as the distinct difference between the deep-seated landslide and the Little Lake watershed morphology (Fig. 1A; Marshall et al., 2016). Topography near the outlet is subdued relative to the surrounding steep, highly dissected terrain. The lack of high-relief terrain in the region separating Little Lake and Triangle Lake, as well as the low-relief hummocky form of the hillslopes bordering Triangle Lake, suggests that multiple deep-seated landslides may have predated the most recent lake-forming landslide. Importantly, the bare-earth LiDAR data allow us to discern continuous beveled surfaces (potential lake levels and terraces), remnants of alluvial-fan deposits, and spillway elevations to constrain the Little Lake depositional history. (Data are available for download and easy interactive three-dimensional viewing at https://dx.doi.org/10.6084/m9.figshare.3545114.)

Based on the elevation of the valley sediments, the paleo–lake level was at least ~40 m higher than Little Lake's present elevation of 217 m above sea level (masl), with continuous paleolake shorelines evident at 260 masl (Figs. 1B–1C). Wave-cut benches, observed in the field and visible on adjoining hillslopes in the LiDAR data, suggest lake levels were as high as 290 masl (Fig. 1B). Little Lake outflows bisect the landslide dam (213 masl) before flowing into Triangle Lake. The bedrock-controlled Triangle Lake outlet (207 masl) discharges into Lake Creek, a large tributary to the Siuslaw River (Fig. 1C). An elevated paleovalley with ~1 m of fluvial gravels and cobbles overlying weathered landslide deposits lies just to the southeast of the modern Little Lake outlet, implying a complex outflow history. This abandoned spillway elevation, similar to the top of the landslide dam (240 m masl), suggests that the paleolake previously drained directly into Lake Creek. Since emplacement of the landslide, the position of Lake Creek shifted eastward onto a bedrock surface upslope of the landslide deposit, which promoted stabilization of the lake level (Fig. 1B).

Little Lake Basin—Previous Paleoenvironmental Findings

Sediment core data (pollen and plant macrofossils) collected from Little Lake by Worona and Whitlock (1995) and again by Grigg et al., (2001) in the distal fen (Fig. 1B) provide continuous records of late Quaternary climate change from 44,700 (43,800–45,800, 2σ range) calibrated yr B.P. (cal yr B.P.) to 250 yr B.P. The core contains a 1-cm-thick layer of well-preserved ash from the Mount Mazama eruption dated at ca. 7.6 ka (Sarna-Wojcicki et al., 1983). The original core analysis subdivided the record into five major climate regimes over the past 43,000 yr (Worona and Whitlock, 1995). Subsequent core analysis (Grigg and Whitlock, 1998, 2002) and new core data from the Little Lake fens (Grigg et al., 2001) provide high-temporal-resolution insight into ecosystem and climatic variability and a detailed paleoclimate reconstruction. These pollen records show that over the last 43 k.y., three distinct forest types existed in the watershed. Pollen data spanning the end of the pre-LGM (MIS 3) chronicle an open-canopy forest assemblage composed of pine (*Pinus* spp.), western hemlock, and fir (*Abies* spp.), with minor amounts of Douglas fir and cedars (Cupressaceae), indicating cooler and wetter conditions than today (~3 °C cooler). During the last glacial interval (MIS 2), the ecosystem consisted of a nutrient-poor, meadow-dominated, spruce (*Picea* spp.), mountain hemlock (*Tsuga mertensiana*), and lodgepole pine (*Pinus contorta*) open parkland, suggesting a colder (by 7–14 °C; Worona and Whitlock, 1995) and drier climate than the modern closed-canopy Douglas fir forest (Grigg et al., 2001). These reconstructions were unable to identify spruce pollen to the species level, leaving unresolved if the climate at Little Lake was most similar to the modern Pacific Northwest Cascades, the Olympics, coastal British Columbia, or maritime southeastern Alaska (Grigg et al., 2001). While the inferred LGM precipitation regime fluctuated between wet and dry, LGM mean annual precipitation was on average ~250–500 mm less than the modern value of 1500 mm (Grigg et al., 2001; PRISM Climate Group, 2016). The lake pollen chronicles a shift toward warm, moist conditions and temperate, closed-canopy Douglas fir forests at 13 ka, coincident with the onset of the modern interglacial interval (MIS 1; Worona and Whitlock, 1995).

THEORETICAL FRAMEWORK—APPARENT VERSUS ACTUAL ^{10}Be-DERIVED EROSION RATES

Cosmogenic Nuclides and Steady State

When deriving erosion rates from CRNs, it is standard practice to model erosion rates as steady, even in transient landscapes (Granger and Riebe, 2014; Heimsath, 2006; Wilkinson and Humphreys, 2005). Under steady erosion, when erosion rates are faster than ~0.1 mm yr^{-1}, we can neglect radioactive decay and calculate CRN concentrations at the surface (assuming no mixing) as:

$$N = \frac{P_s L}{D}, \quad (1)$$

where P_s is the surface nuclide production rate by nucleon spallation (atoms M^{-1} T^{-1}), L is the attenuation length (M L^{-2}), and D is the denudation rate (M L^{-2} T^{-1}; Granger and Riebe, 2014; Lal, 1991). Note that Equation 1 ignores production by muons for simplicity. They can be easily incorporated using a multiple exponential approximation for their production rate with depth (for a detailed explanation, see Granger and Riebe, 2014).

Terrestrial in situ cosmogenic nuclides such as ^{10}Be, ^{26}Al, and ^{3}He are standard tools for dating rock surfaces and calculating soil production and erosion rates (see Granger and Riebe, 2014; Lal, 1991; von Blanckenburg, 2005). As cosmic rays bombard Earth's surface, they produce a cascade of secondary particles that collide with the nuclei within minerals to produce rare cosmogenic nuclides. When bedrock is exhumed by surface erosion and exposed to sec-

ondary cosmic rays, minerals such as quartz accumulate cosmogenic nuclides as they approach the surface. Production by neutron spallation dominates in the uppermost few meters near the ground surface. Production at greater depths continues due to production by negative muon capture and fast muon reactions. These reactions do not have a simple exponential attenuation length, although they can be approximated as the sum of several exponentials (e.g., Granger and Muzikar, 2001).

Erosion rates derived from cosmogenic nuclides such as ^{10}Be are relatively insensitive to anthropogenic influences on erosion in the recently settled western United States, as well as short-term (<1000 yr) climate fluctuations (von Blanckenburg, 2005). In moderately eroding sites such as the OCR, ^{10}Be concentrations integrate erosion rates over millennial time scales. For rock with a density of 2.1 g cm^{-3}, such as the bedrock at our study site, the effective attenuation length corresponds to a depth of 76 cm. Specifically, with an attenuation length of 76 cm and an erosion rate of 0.1 mm yr^{-1}, ^{10}Be integrates erosion rates over a time scale of 7600 yr, exponentially weighted toward the present (Lal, 1991).

Because cosmogenic-derived erosion rates integrate information over thousands of years, the assumption of steady erosion leads to an overestimate of true erosion rates when erosion rates are slowing over time, and an underestimate of true erosion rates when erosion rates are increasing (Granger and Riebe, 2014; Lal, 1991; von Blanckenburg, 2005). Not only can apparent erosion rates deviate from actual erosion rates due to changing soil production rates, but as discussed later herein, changes in the soil mixing depth can also differentiate CRN inventories in soil and the underlying bedrock, which can lead to underestimates or overestimates of actual erosion rates.

Transient Erosion and Soil Mixing Depths

Most soils undergo some form of mixing, with the depth and vigor dependent on climate-dependent disturbance processes (e.g., tree throw, burrowing, earthworm activity, frost heave). Therefore, it is reasonable to expect that as climate changes, soil production processes and the associated mixing depths could also change.

Following Granger and Riebe (2014) and Heimsath (2006) in assuming negligible radioactive decay and soil production rates equal to total denudation rates (i.e., $D_{soil} = D = P$), we can conceptualize the average nuclide concentration in the mixed soil using the following equation:

$$\frac{d\langle N\rangle}{dt} = \langle P\rangle - \frac{\langle N\rangle D}{\rho h} + \frac{N_{saprolite} D}{\rho h}, \quad (2)$$

where $\langle\ \rangle$ denotes depth-averaged in the homogeneous, well-mixed soil, N is the nuclide concentration (atoms M^{-1} T^{-1}), ρ is the average density of the mixed layer (M L^{-3}), P is the depth-dependent spallogenic production rate, and h is soil depth (Fig. 2A). This is similar to the model for a well-mixed eroding surface used by Granger et al. (1996), except we allow mixing depth to vary with time. Similar to Granger et al. (1996), we treat mixing as homogeneous and instantaneous. Essentially, the rate of nuclide concentration change depends on nuclide production in the soil (term 1), the loss due to erosion (term 2), and input from underlying bedrock or saprolite (term 3). If the mixing depth increases (e.g., from h_1 to h_2), then the average soil concentration "instantaneously" decreases as material from depth is injected into the mixing zone (Fig. 2B), which can result in a sudden spike in apparent erosion rates that exceed the actual erosion rates. Conversely, if $h_2 < h_1$, new saprolite or bedrock will not be incorporated into the soil column until denudation removes the overlying soil to a thickness equal to h_1-h_2 (Fig. 2B). For simplicity, Equation 2 only accounts for production by spallation because the penetration length for spallation reactions (76 cm in rock of density 2.1 g cm^{-3}) is comparable to soil mixing depths, while the penetration lengths for muon reactions are much longer and are not as significantly affected by changes in soil mixing depth.

Note that the steady solution commonly used to determine erosion rates (Eq. 1) does not depend on the mixing depth. By contrast, Equation 2 includes soil depth and indicates that as soil depth increases, nuclide concentrations in the soil take longer to adjust. As several previous workers have demonstrated (Heimsath, 2006; Lal, 1991; Schaller and Ehlers, 2006; von Blanckenburg, 2005), there is a lag time between actual and apparent nuclide-derived erosion rates under transient conditions, as cosmogenic-derived erosion rates integrate information over thousands of years. However, due consideration has not been given to the importance of variable mixing depths in terms for interpreting cosmogenic nuclide concentrations.

Apparent versus Actual ^{10}Be-Derived Erosion Rates under Transient Conditions

To illustrate how CRN-derived (apparent) erosion rates deviate from actual erosion rates in a transient, soil-mantled setting, we solved Equation 2 for varying erosion rates and mixing depths that change over 20 k.y. intervals for 120 k.y. For the first 60 k.y., actual erosion rates vary by a factor of 3, fluctuating between 0.3 mm yr^{-1} and 0.1 mm yr^{-1}. For the next 60 k.y., the actual erosion rates fluctuate by a factor of 1.5, varying between 0.15 mm yr^{-1} and 0.1 mm yr^{-1} (Fig. 3).

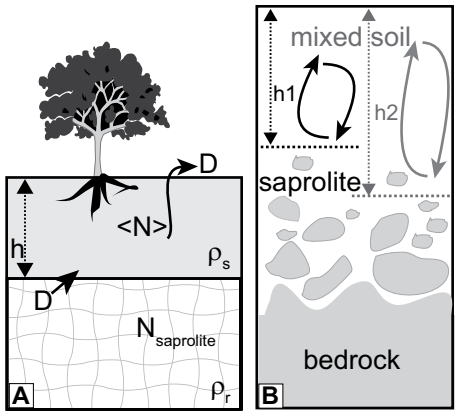

Figure 2. Models of cosmogenic nuclide accumulation and loss in vertically well-mixed soils. (A) Conceptual model illustrating cosmogenic nuclide accumulation and loss in a well-mixed soil (Eq. 2), where *N* is nuclide concentration (atoms M^{-1} T^{-1}), < > denotes depth-averaged, *D* is the denudation rate (M L^{-2} T^{-1}), and ρ_r and ρ_s denote rock and soil density (M L^{-3}), respectively. (B) Model illustrating how increasing the mixing depth (h_1 to h_2) incorporates weathered bedrock with lower nuclide concentrations into the soil nuclide inventory. Figure is modified from Granger and Riebe (2014).

First, we model the actual and apparent erosion rates for two scenarios with constant mixing depths of 20 cm and 60 cm (Fig. 3A). The greater the increase in erosion rates, the faster this change occurs if the mixing depth is shallow; a 3× increase in actual erosion takes ~15 k.y. for the soil to integrate the perturbation given a mixing depth of 20 cm.

Next, we evaluate apparent erosion rates with fluctuating moderate (60 cm) and deep (120 cm) mixing depths. We present two opposing mixing depth scenarios; in one scenario, mixing depths and erosion rates increase or decrease concurrently (scenario A), while in the second scenario, we reverse the mixing depths such that deeper mixing depths are paired with the slower erosion rates (scenario B; Fig. 3B, dark-gray dashed line for scenario A and light-gray dashed line for scenario B). In these model scenarios, an increase in mixing depth can generate a spike in apparent erosion, which often exceeds the actual erosion rate, as low concentration material is incorporated into the newly thickened soil column. The erosion rate spike decays rapidly following this instantaneous input when there is

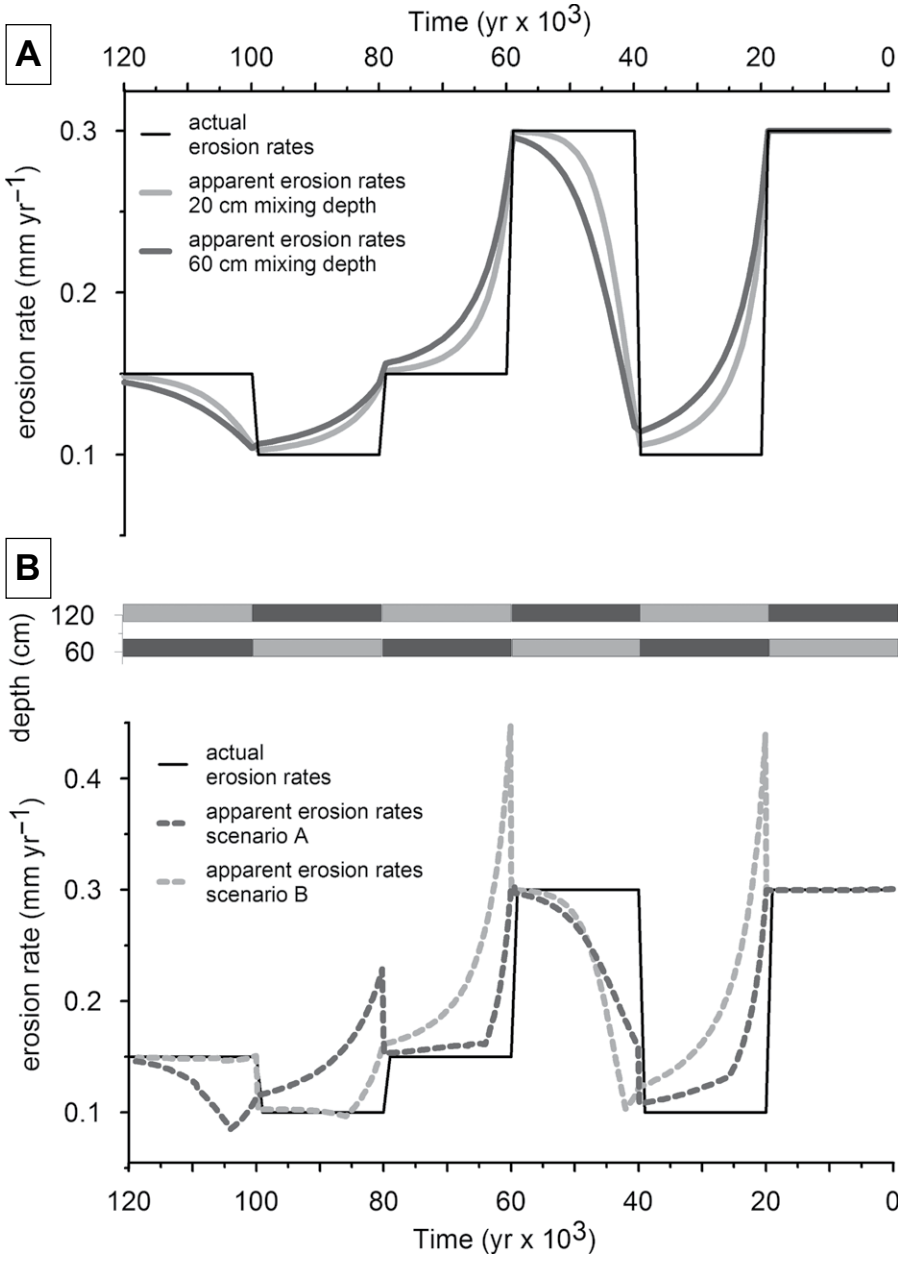

Figure 3. (A) Model applying the transient solution for nuclide-derived erosion rates with fluctuating erosion rates and mixing depths of 20 cm (light-gray line) and 60 cm (dark-gray line). Black solid line delineates the actual erosion rates through time. (B) Transient erosion rate and mixing model output with fluctuating mixing depths of 60 cm and 120 cm. In scenario A (dark-gray dotted line), mixing depths and erosion rates co-increase and co-decrease. In scenario B (light-gray dotted line), mixing depths increase when erosion rates increase. Mixing depths for each scenario's time interval are represented by alternating dark-gray (scenario A) and light-gray (scenario B) rectangles in horizontal bars above lower plot. Note: Minimum value on *y*-axes is 0.05 mm yr^{-1}.

a commensurate and significant decrease in the erosion rate (see scenario B at 20 and 60 k.y. in Fig. 3B). Apparent erosion rates adjust faster to transient changes when erosion rates and mixing depths either increase (scenario B at 100 k.y.) or decrease concurrently (scenario A at 20 k.y. and 60 k.y. in Fig. 3B). Additionally, when erosion rates increase and mixing depth decreases, a transient excursion in apparent erosion rates occurs as remnant soils previously mixed with a slower erosion rate are exhumed (e.g., $h_2 < h_1$ in Fig. 2B). Once the remnant soils are removed (e.g., the soil depth = h_2), apparent erosion rates rapidly approach the actual erosion rates (scenario B at 40 k.y. and 100 k.y. in Fig. 3B). Importantly, the apparent erosion rates depend on the magnitude of the imposed mixing depth, and the overshoot behavior depends on the relative magnitude of the depth increase compared with the erosion rate increase.

METHODS

Core Collection and Processing

We chose our primary sediment core location upstream of the modern lake to satisfy the following criteria and considerations. Given our principal goal of deriving erosion rates from quartz-rich sediments, we sought to maximize the likelihood of sampling hillslope-derived sediments and thus set our core location in the central valley axis proximal to the sediment source area (Fig. 1B). Specifically, we required sufficient quartz mass within a <4-cm-diameter sampling tube to obtain erosion rates over short (<1000 yr) time intervals from sediments with a size range of 0.25–2 mm. This criterion differs significantly from typical lake sediment coring efforts, including those at Little Lake, which target fine sediments for maximum fossil preservation.

We collected near-continuous samples from the paleolake surface to 63 m depth, with the final core-drive into saprolite underlying the valley lake fill. Our primary core data come from a cluster of three drill holes, relying mainly on truck-mounted drills (cores NOB A-C) and hand drilling with a Livingston corer (NOB I).

At our primary sample site, NOB, we initially employed a truck-mounted, hollow-stem auger continuous sampling system (core NOB A, 44.16876°N, 123.59436°W). Our first core drive began 5 ft (1.52 m) below the surface, with poor recovery in our first two drive attempts (5–15 ft, 1.52–4.57 m). Sediment only partially filled the sample tubes, and the gaps in the core segment precluded the precise depth control necessary to develop a consistent depth-age model. We drilled to 85 ft (25.91m), with increasingly poor to no recovery.

To increase recovery, we switched to a truck-mounted, mud-rotary drill for an adjacent core recovery effort (NOB B, 44.16867°N, 123.59434°W). The setup utilized a 2 ft (0.61 m) California split-spoon sampler encasing four stacked brass or stainless-steel tubes, each 0.5 ft (0.15 m) long and 1.5 in. (3.81 cm) in diameter. Based on well log data and one-dimensional reconstructions of the paleovalley topography, we estimated the deposit depth at ~60 m. Therefore, we subsampled the upper 29 m of paleosedi-

ments, with continuous sampling from 30 m downward, in 2 ft (0.61 m) increments.

We again employed a mud-rotary drill at our main sample site (NOB) to subsample intervals from 12 ft (3.66 m) to 111 ft (33.83 m) (NOB C, 44.16862°N, 123.59435°W) to cross-validate sample depths in the NOB B core. We also collected hand-augered samples (NOB I) from the surface to 3.65 m before the onset of the mechanical drilling operation. In an effort to collect contiguous paleosediments from the late Pleistocene through the Holocene, we hand augered at a site closer to the upstream end of modern Little Lake (LIT, 44.16735°N, 123.58668°W; Fig. 1B), using the combination of a soil auger and Livingston corer. Compacted fine sediments halted our efforts at 7.9 m below the surface.

All sample intervals, whether extracted manually or mechanically, were logged and labeled onsite and tightly wrapped in plastic before sealing with tape.

In order to extract the tightly packed sediment deposits from the 269 sample tubes without disturbing the sediments, we carefully slit each metal casing lengthwise, using a custom-built jig and a horizontal bandsaw fitted with a vacuum nozzle to prevent metal shaving contamination. To extract the sediments, we used a custom-built extruder. We preserved core chronology by laying the split cylinders end to end in split polyvinyl chloride (PVC) tubes. We visually described each core segment, noting changes in color, laminations, concretions, grain-size information, and plant macrofossils. Once logged, labeled, and wrapped, we encased the cores in protective plastic tubes, color coded as working or archive, and transferred them to a temperature-controlled cooler.

Because of the mud-rotary drilling method (NOB B and C), ~10% of the 269 samples had no recovery or contained driller's mud in the upper centimeters of the sample sequence. When present, the driller's mud was confined to a thin (~<2 cm) layer above the sediments in a sample tube rather than coating the tightly packed sediments, and thus was easily avoided when describing the cores.

Core Dating and Plant Macrofossil Analysis

We adopted an iterative sample dating strategy, initially extracting plant macrofossils from the upper part of the core for radiocarbon dating and identification while processing quartz sediments from deeper in the core using optically stimulated luminescence (OSL) dating methods. In total, we extracted 25 plant macrofossils from the core for ^{14}C dating and three sediment segments for OSL dating in order to construct depth-age models (Tables 1 and 2). OSL samples remained encased in steel sample tubes until analysis.

We extracted and processed all plant macrofossils for accelerator mass spectrometry (AMS) ^{14}C dating using standard pretreatment techniques involving 10% KOH and 10% HCl rinses. Whenever possible, we dated single macrofossils. When we were unable to find single specimens in the depth of interest, we sought fragments in close proximity with one another to minimize uncertainty (Table 1). To refine previous paleoclimate reconstructions, we extracted plant macrofossils from additional subsamples (100–250 cm^3) targeted at 68 depths containing organic-rich sediments. We identified macrofossils under a binocular stereoscope using published keys (Dunwiddie, 1985) and a reference collection.

We generated two depth-age models. To assign ages to each core segment, we used a monotonic spline fit to the measured depths and the best-modeled median calibrated ages (Table 1), generated with the CLAM model (ver. 2.2, http://chrono.qub.ac.uk/blaauw/clam.htm; Blaauw, 2010). The spline fit model describes local sediment accumulation rates at each depth interval. As regression models

TABLE 1. ^{14}C DATA

Sample ID*	CAMS ID	Material dated	Depth (m)	^{14}C age (yr)	Error (yr)	Min 95% (cal k.y. B.P.)	Max 95% (cal k.y. B.P.)	Median (cal k.y. B.P.)
Radiocarbon dates used in depth-age model and for constraining CRN sample age								
LIT I-D	160860	Charcoal (1 fragment)	–1.15	3090	30	3.23	3.38	3.30
LIT I-L	156944	Wood (1 fragment)	–2.17	2425	25	2.35	2.69	2.45
I-P	155165	Wood (1 fragment)	–3.22	18,500	50	22.26	22.52	22.39
C14tip	155166	Wood (1 fragment)	–4.57	19,030	50	22.67	23.14	22.91
C20tip	152768	Wood (1 fragment)	–6.40	19,390	70	23.07	23.60	23.35
C40tip	153571	Small pieces of wood	–12.50	19,410	60	23.10	23.61	23.38
C60tip	153573	Wood (1 fragment)	–18.59	19,720	70	23.51	24.00	23.75
B60d*	159909	Charcoal (1 fragment)	–18.59	26,600	800	28.86	32.24	30.60
B74c	156945	Wood (1 fragment)	–22.82	20,150	70	23.99	24.44	24.22
C83a	156946	Wood (1 fragment)	–25.15	21,030	80	25.15	25.61	25.39
B96tip	156032	Wood (1 fragment)	–29.69	21,425	45	25.61	25.89	25.76
B114tip	158582	Wood (2 fragments)	–36.28	23,880	150	27.66	28.30	27.93
B126d	160069	Wood (several fragments)	–40.69	25,790	130	29.54	30.46	30.00
B126tip†	158585	Wood (1 fragment)	–40.83	25,880	180	29.57	30.64	30.11
B140tip	156032	Charcoal (1 fragment)	–46.12	31,310	110	34.85	35.52	35.17
B156d	158584	Wood (1 fragment)	–51.85	32,970	420	36.14	38.34	37.14
B158b	160070	Wood (several fragments)	–52.31	33,900	360	37.09	39.17	38.33
B174b	158581	Wood and bark (1 fragment)	–57.63	40,330	1030	42.42	45.63	43.96
B207a	160071	Wood (1 fragment)	–63.2	45,590	1480	46.19	>50.00	48.43
B207a†	158586	Wood (1 fragment)	–63.2	46,780	2280	n/a	n/a	n/a
Radiocarbon dates not used (assumed redeposited)								
A2–33†	158583	Charcoal	–2.54	13,590	560	14.62	17.94	16.37
A4–28†	158571	Charcoal	–3.33	16,710	60	19.96	20.37	20.16
C50a	159908	Wood (1 fragment)	–15.24	28,610	220	31.82	33.35	32.65
C50tip	153572	Wood (several small pieces)	–15.54	21,130	80	25.23	25.69	25.48
C91b	159910	Wood (1 fragment)	–27.89	21,690	100	25.76	26.12	25.94
C91c	158580	Wood (1 twig)	–28.04	25,790	180	29.48	30.56	30.01
C100tip	155167	Wood (1 fragment)	–30.78	23,980	90	27.76	28.29	28.00
B158a	158592	Needle and wood	–52.16	31,830	370	34.91	36.43	35.71

Note: All samples were processed at Lawrence Livermore National Laboratories Center for Accelerator Mass Spectrometry (CAMS). Radiocarbon dates were calibrated using the INTCAL13 calibration curve using CALIB 7.10 (Reimer et al., 2013). CRN—cosmogenic radionuclide.

*All samples were collected from NOB, our primary sample site, with the exception of LIT I-D and LIT I-L, which we collected at our secondary site upstream of modern Little Lake (see Fig. 1B and Methods—Core Collection section).

†Dates excluded from depth-age models in preference of adjacent date with lower error.

TABLE 2. OPTICALLY STIMULATED LUMINESCENCE (OSL) INFORMATION

Sample	USU ID	Aliquots (*n*)	Equivalent dose, De (Gy)	Overdispersion (%)	Dose rate (Gy/ka)	OSL age (ka)
Age information*						
B110b	USU-983	**27** (55)	63.08 ± 7.92	31.2 ± 4.6	31.2 ± 4.6	31.2 ± 4.6
B136b	USU-974	**28** (43)	81.26 ± 7.58	24.3 ± 3.4	2.35 ± 0.19	34.51 ± 4.54
B168c	USU-975a	**27** (34)	92.62 ± 6.68	18.0 ± 2.6	2.26 ± 0.24	40.92 ± 5.64
Sample	Depth (m)	H_2O^3 (%)	U (ppm)	Th (ppm)	K (%)	Rb (ppm)
Dose rate information†						
B110b	33.7	34.7	2.3 ± 0.2	11.7 ± 1.1	1.90 ± 0.05	82.8 ± 3.3
B136b	41.5	29.4	1.7 ± 0.1	9.4 ± 0.9	2.05 ± 0.05	82.8 ± 3.3
B168c	55.9	45.4	3.1 ± 0.2	13.9 ± 1.3	1.69 ± 0.04	90.6 ± 3.6

*Age analysis using the single-aliquot regenerative-dose procedure of Murray and Wintle (2003) on 2 mm small aliquots (SA) of quartz sand. Number of aliquots used for age calculation is in bold; number of aliquots measured is in parentheses. Overdispersion represents scatter in De beyond calculated uncertainties in data; overdispersion >20% is considered significant. Error on age is 2σ standard error.

†H_2O^3 refers to in situ moisture content. Contribution of cosmic radiation is 0, due to the deep-water setting. Grain size for all samples was 63–50 µm. All samples were processed at the Utah State University Luminescence Laboratory.

better describe sediment accumulation trends and deviations, we also constructed a depth-age model using two linear regression equations fit above and below an inflection point in the data between 36 m and 41 m (Fig. 4). We did not include five anomalously old samples (age-reversed) in either depth-age model, as the negative excursions reflected either remobilized lakeside sediments or turbated lake sediments (Fig. 4; Table 1).

Cosmogenic Nuclide Sample Selection and Processing

To select samples for cosmogenic nuclide analysis, we used our depth-age models and textural grain-size observations to maximize temporal resolution and avoid potential debris-flow deposits. We also focused our sampling on depths with distinct changes in sediment accumulation rates and at the transitions across climate intervals. We used amalgamated sediments from the shortest time interval possible (<1000 yr), given mass requirements to extract sufficient quartz grains ranging in size from 0.25 to 2 mm for cosmogenic nuclide analysis. We processed 27 samples, each of which integrated deposits over 700 yr or less based on the relevant sedimentation rate. We also collected modern catchment-averaged sediment samples from two tributary streams above the influence of the paleolake (Fig. 1B; Table 3).

All CRN samples were processed using standard techniques at the Purdue Rare Isotope Measurement (PRIME) Laboratory. After sieving sediments, we separated quartz from the samples and isolated ^{10}Be following procedures modified from Kohl and Nishiizumi (1992). All samples went through a series of quartz physical preparation steps, including selective leaching in dilute HF/HNO_3, froth flotation, and magnetic separation to eliminate other minerals and any meteoric ^{10}Be. After physical separation, the samples were spiked with a beryllium carrier solution and dissolved in HF/HNO_3. We separated the beryllium on a cation exchange resin in oxalic acid following selective precipitation. Beryllium hydroxide was converted to nitrate and decomposed by flame. Beryllium oxide was mixed with niobium powder and loaded into stainless-steel holders for analysis by AMS. For more details on the methods, see http://science.purdue.edu/primelab/user-information/quality-control.php. AMS measurements were made at the PRIME Laboratory referenced against standards prepared by K. Nishiizumi (Nishiizumi et al., 2007).

Erosion Rate Calculations

We determined apparent erosion rates for both lake core and modern stream samples using a production rate scaling model that spatially averages ^{10}Be production rates weighted by basin hypsometry. Because sedimentological evidence in the core and both field and LiDAR-derived evidence of terraces 40–50 m above the lake bottom support a deep-water setting (Fig. 1; Marshall et al., 2016) that would rapidly attenuate postdeposition cosmic rays, we did not correct for nuclide production during or after sediment deposition. We assumed that production rates were steady over time and calculated average production rates

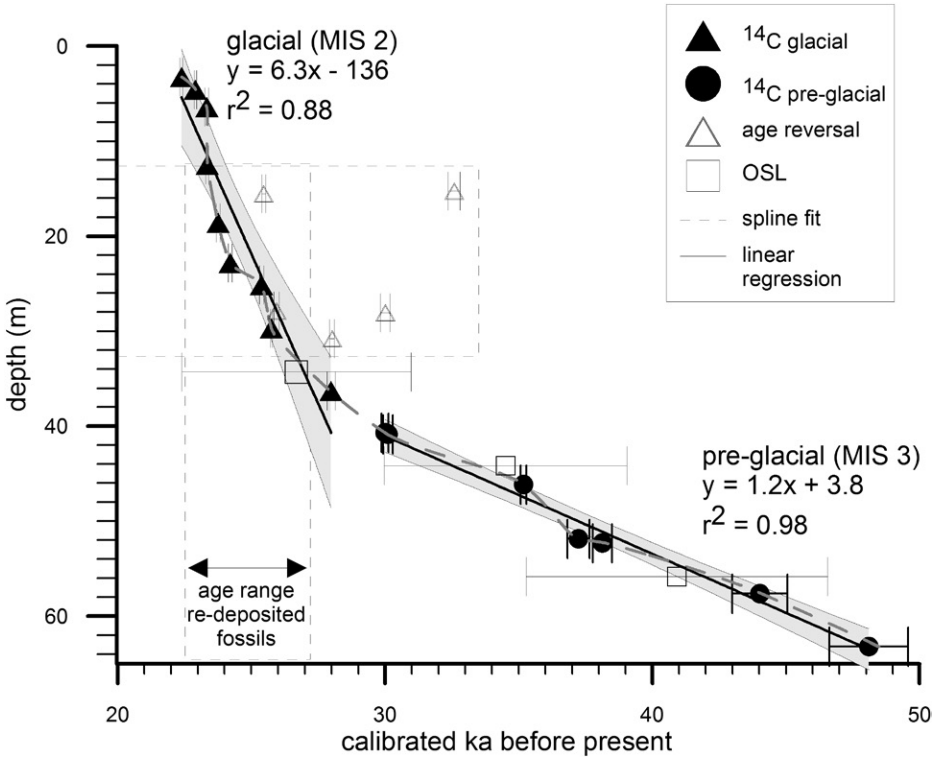

Figure 4. Depth-age model based on ^{14}C and optically stimulated luminescence (OSL) dates. Linear fits (solid lines) describe the trends in sediment accumulation rates over time. Cubic spline fit is shown with a dashed line and describes local accumulation at each depth interval. Open triangles mark fossils with dates chronologically older than underlying fossils (age-reversed). Dashed boxes show the relationship between age-reversed fossils (horizontal box) and age of the surrounding sediments based on our depth-age models (vertical box). MIS—marine isotope stage.

TABLE 3. COSMOGENIC NUCLIDE DATA AND CALCULATED EROSION RATES

Sample	PRIME ID	Qz mass (g)	Be mass (µg)	$^{10}Be/^{9}Be$ (10^{-15})	Blank* (10^{3} at g^{-1})	[^{10}Be] (10^{3} at g^{-1})	Erosion rate† (mm yr^{-1})	Core depth (m)	Age (ka)
Paleolake samples									
LIT I-D	201201530	22.76	284.46	76 ± 5	10.5 ± 1.2	43.5 ± 3.6	0.12 ± 0.01	1.15	ca. *1.5*§
LIT I-L	201201865	14.70	265.22	44 ± 7	10.0 ± 1.4	43.1 ± 8.6	0.12 ± 0.02	2.17	2.43
A2	201201867	27.75	270.14	64 ± 3	5.3 ± 0.8	36.1 ± 2.2	0.14 ± 0.01	2.54	ca. *6.0*§
A4	201201866	24.07	273.24	53 ± 4	6.1 ± 0.9	33.9 ± 2.9	0.15 ± 0.01	3.33	ca. *7.5*§
C14b#	201201498	5.79	283.71	15 ± 1	41.3 ± 4.8	8 ± 6.6	0.64 ± 0.52	4.27	22.60
C20b	201201500	22.41	284.8	44 ± 5	10.7 ± 1.2	26.8 ± 4.4	0.19 ± 0.03	6.25	23.33
C23b+c	201201501	16.32	260.0	39 ± 3	14.6 ± 1.7	26.6 ± 3.4	0.19 ± 0.03	7.16	23.35
C30b+tip	201201502	30.72	255.2	57 ± 4	7.8 ± 0.9	23.9 ± 2.4	0.21 ± 0.02	9.45	23.56
C51b	201201504	17.67	284.89	50 ± 3	13.5 ± 1.6	40.1 ± 3.4	0.13 ± 0.01	15.7	23.53
B60c	201201505	13.99	275.27	39 ± 3	17.1 ± 2.0	34.3 ± 4.4	0.15 ± 0.02	18.44	23.74
C70b	201201506	17.57	285.10	41 ± 3	13.6 ± 1.6	30.9 ± 3.6	0.17 ± 0.02	21.49	24.01
B74c	201201507	15.59	256.13	43 ± 3	15.3 ± 1.8	32.0 ± 3.8	0.16 ± 0.02	22.82	24.22
C83a	201201508	14.14	253.89	43 ± 9	16.9 ± 2.0	32.0 ± 3.8	0.15 ± 0.05	25.15	25.39
C90tip#	201201510	9.39	254.32	49 ± 18	25.5 ± 3.0	62.5 ± 32.3	0.08 ± 0.04	27.74	25.58
C93c	201201512	16.63	257.3	37 ± 4	14.4 ± 1.7	23.9 ± 4.4	0.21 ± 0.04	28.50	25.64
B96d	201201513	18.65	258.9	42 ± 4	12.8 ± 1.5	26.2 ± 4.0	0.20 ± 0.03	28.96	25.67
C103a	201201515	12.52	285.6	27 ± 5	19.1 ± 2.2	22.1 ± 8.0	0.23 ± 0.08	31.24	26.70
B112	201201870	13.83	272.81	18 ± 3	10.6 ± 1.5	14.6 ± 4.2	0.35 ± 0.10	35.21	23.74
B118b+c	201201516	15.46	271.2	32 ± 5	15.5 ± 1.8	22.1 ± 6.1	0.22 ± 0.06	37.50	28.48
B122d	201201517	15.33	255.38	46 ± 6	15.6 ± 1.8	35.7 ± 6.9	0.14 ± 0.03	39.26	29.36
B124c	201201518	15.75	258.91	46 ± 4	15.2 ± 1.8	35.4 ± 4.7	0.14 ± 0.02	39.84	29.64
B128b#	201201519	12.73	256.56	37 ± 17	18.8 ± 2.2	30.7 ± 17	0.17 ± 0.13	41.17	30.23
B148d	201201522	6.99	253.35	20 ± 2	34.2 ± 4.0	14.3 ± 6.2	0.36 ± 0.15	49.06	36.20
B154b	201201523	11.07	262.01	31 ± 4	21.6 ± 2.5	27.5 ± 6.8	0.19 ± 0.05	50.70	36.70
B166	201201524	15.82	284.78	36 ± 3	15.1 ± 1.8	28.3 ± 4.0	0.18 ± 0.03	54.98	41.47
B176	201201525	15.59	284.57	48 ± 5	239 ± 28	43.3 ± 6.4	0.18 ± 0.03	58.42	44.76
B197	201201526	9.82	259.48	60 ± 14	239 ± 28	81.7 ± 24.9	0.06 ± 0.02	60.43	46.36
Tributary samples									
Trib 1	201201864	12.85	274.2	63 ± 7	147 ± 21	53.8 ± 7.3	0.10 ± 0.01	n/a	n/a
Trib 2	201201863	20.05	269.2	68 ± 8	147 ± 21	78.6 ± 10.1	0.07 ± 0.01	n/a	n/a

Note: Bedrock density for all samples is 2.0 g cm^{-3}.

*The ^{10}Be samples reported here suffered from an unusually high blank because of contamination in the chemistry laboratory. Although the level of contamination was high, it was highly reproducible. The core samples reported here were bracketed by four different blanks, two of which were analyzed twice. The tributary samples were run separately and were bracketed by two different blanks. We corrected the concentrations of ^{10}Be for the contamination by subtracting a fixed number of ^{10}Be atoms regardless of sample mass. The laboratory contamination has since been corrected.

†Uncertainties in erosion rate reflect errors in accelerator mass spectrometry measurements of samples and blanks and do not include uncertainties in production rates.

§Estimated sample depth based on position above Mount Mazama tephra (ca. 7.6 ka).

#Reported but unused value due to low nuclide concentration combined with high uncertainty.

using the CRONUS calculator (http://hess.ess.washington.edu; Balco et al., 2008). To evaluate whether the assumption of steady production was appropriate, we examined production rates using the time-varying model of Lifton et al. (2009). We smoothed production rates using an 8000 yr moving average to represent the production rates over the sediment irradiation history and found that over the time interval from 50 to 20 ka, production rates varied by only ~5% and were similar to production rates averaged over the past 8000 yr. Thus, the assumption of steady production holds for variability of the geomagnetic field.

For all core samples, we used a surface spallogenic production rate, P_s, of 5.92 at g^{-1} yr^{-1}; Trib 1 and Trib 2 (our stream samples) have spallogenic production rates of 6.42 and 6.69 at g^{-1} yr^{-1}, respectively. We estimated production due to muons following a multi-exponential profile from previous work (Granger and Muzikar, 2001), using revised muon production cross sections (Borchers et al., 2016). We also ignored quartz enrichment due to chemical erosion, because this is only important in sites with intense chemical weathering (Granger and Riebe, 2014; Riebe et al., 2001c). Chemical weathering is low in the modern warm and wet Oregon Coast Range (Almond et al., 2007; Anderson, 1998), and thus the colder and drier LGM chemical weathering regime is expected to have been low. All reported means are weighted by inverse variance.

Cosmogenic nuclide analysis requires subtraction of a process blank to account for the small amount of ^{10}Be introduced in the laboratory. At the time our samples were processed, there was an unusually high process blank due to contaminated reagents in the chemistry laboratory. Although the blank was high, it was reproducible for all samples processed at this time, so we can confidently subtract the blank value from our measurements. This subtraction, together with the low ^{10}Be concentrations in the samples, led to unusually high uncertainties for some of our erosion rates (10%–30%; Table 3).

RESULTS

Next, we describe our visual observations of core data, and then we present ^{14}C and OSL, fossil identification, and cosmogenic nuclide results. Figure 5 summarizes the NOB core data, including plant macrofossil ages for depth intervals in the core, fossil occurrences of note, grain-size data, ^{10}Be-derived erosion rate data, and data relationships to other relevant Little Lake studies.

Core Observations

The entire NOB B and C core sequence is lacustrine, with laminated, predominately clay and sand deposits throughout. The most-striking observation along the length of the core is the profound shift in sediment size, color, and lamination spacing at ~31 m depth (Fig. 5). Below 31 m, the core deposits are generally characterized by finely laminated, mixed clay- to sand-size sediments, varying in color from brown to gray to red. At 31 m, the lake deposits abruptly change to predominantly centimeter-scale laminations and blue-gray, coarse, uniform, subangular sand deposits. The striking subangular blue-gray deposits persist in the core up to ~4 m depth.

Throughout the core, we observed vivianite, a phosphate mineral formed under reducing redox conditions (Rosenqvist, 1970) and commonly found in lacustrine deposits. The deposits fluctuate from gray to brown to red, with laminations and/or thin (millimeter to centimeter scale) lenses of different colors and/or grain sizes within thicker sequences. Gravels, while interspersed throughout the core, never dominate any of the grain-size percentages. Intermittently throughout the core, we observed poorly sorted, matrix-supported deposits (likely originating from debris flows), marked by woody debris and angular clasts.

The deepest segment of the B core (61.6–62.1 m below the surface) contains large, angular, gleyed, deeply weathered clasts, and large pieces of wood jumbled with coarse, poorly sorted sands and clays, which may represent distal deposits of the damming landslide. The landslide deposit overlies a paleosol composed of clay with fine sand, small fragments of wood and charcoal throughout, and a well-preserved core-spanning fragment of wood at 63.20 m. Below the paleosols and forest wood, our basal samples (63.35–63.65 m) are intact, competent sandstone, which likely represents the paleo–valley floor.

We observed tephra deposits at two depths in the cores. First, we found waterlain ash (57 m) below pockets of ash (56.5 m). Second, we

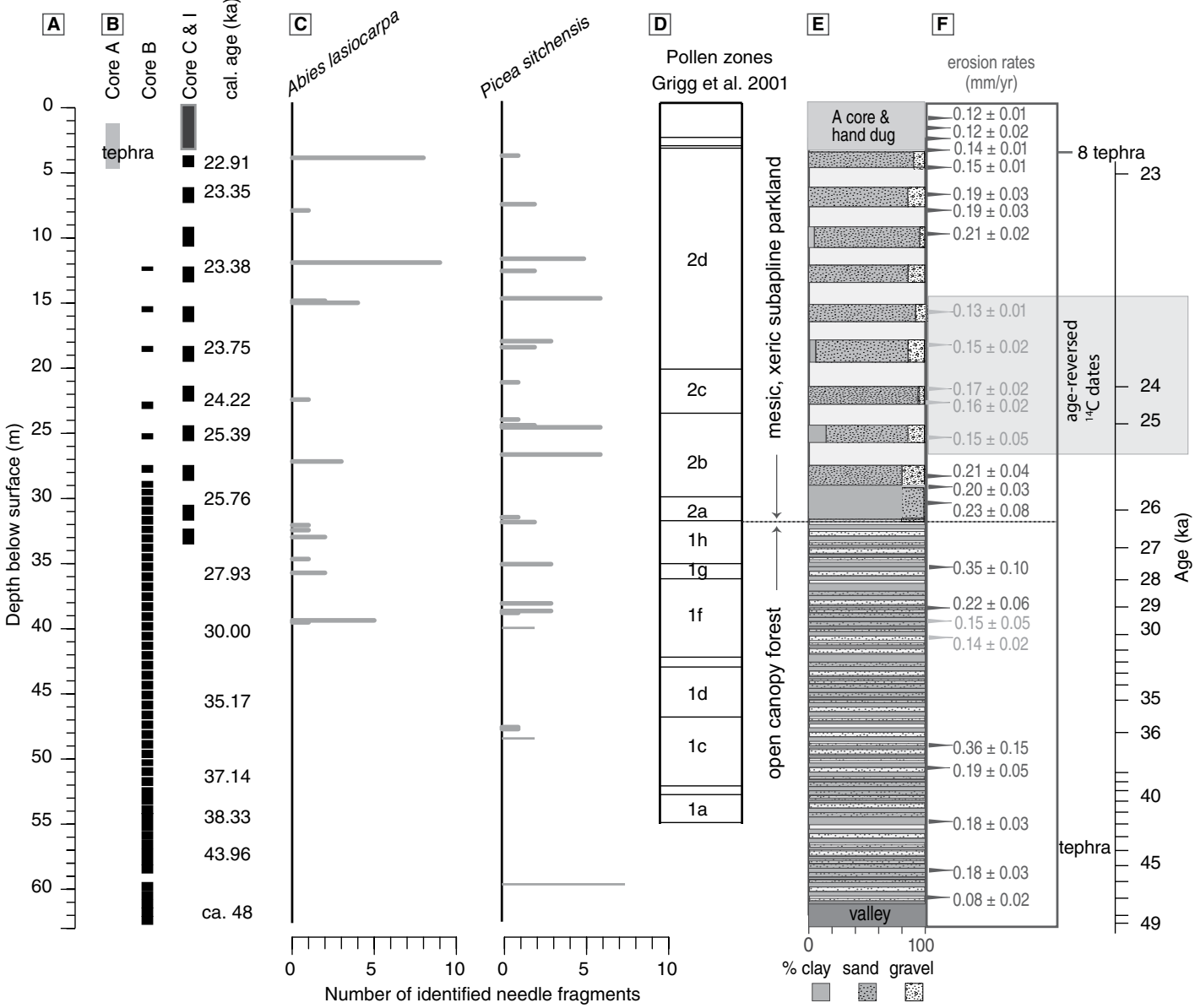

Figure 5. Compilation of Little Lake core observations and data. (A) NOB core sample interval depths described by rectangles. NOB A (gray rectangle, left side of figure) core data lack precise depth control due to gaps in the collection tubes. (B) Radiocarbon dates and depths. (C) *Picea sitchensis* (Sitka spruce) and *Abies lasiocarpa* (subalpine fir) co-occurrence observed at 29.5–22.6 ka based on depth-age model. (See supplemental materials [text footnote 1] for complete macrofossil identification and depths.) (D) Pollen zones of Grigg et al. (2001) and general descriptions of ecosystem types during marine isotope stage (MIS) 3 (LL-1) and MIS 2 (LL-2). (E) Percent clay, sand, and silt in the core based on visual observations. Solid light-gray regions within core stratigraphy column represent intervals without data (replicating gaps in the core described on the left-most side of the figure). Entire core sequence consists of millimeter- to centimeter-scale laminated lacustrine deposits, with a significant reduction in fine-scale laminations, increase in grain size, and increase in sediment accumulation rates at ca. 27 ka, coincident with the start of pollen zone LL-2. Stratigraphy for zone LL-1 is representative but not precise. (F) ^{10}Be-derived erosion rates values in gray have high ^{10}Be concentrations (see Discussion—Lake History). Age range for cluster of age-reversed (redeposited) ^{14}C dates is shaded gray.

observe tephra in both the NOB A and NOB I cores, our two near-surface cores. We have excellent depth control on the hand-dug NOB I samples, where we found a 1-cm-thick ash within lake sediments at 2.93 m below the surface. While our depth control on the NOB A cores was not optimal because the paired 2.5 ft (0.76 m) drives (for a total of 5 ft or 1.52 m) were only partially filled with sediment, we did observe a sharp transition to ash in the A4 tube, at ~4.1 m, with the upper A3 tube bereft of lake deposits. Based on our NOB A core observations, we expect that the deposit was originally emplaced in the A3 tube, which would place the ash at a similar depth below the surface as our hand-dug NOB I core.

Of the 68 samples sieved, 40 contained identifiable macrofossils. We made 175 identifica-

tions to the species level and identified a major transition around 29 ka (Fig. 5; supplemental material[1]). We refine previous Little Lake paleoenvironmental reconstructions (Grigg et al., 2001; Worona and Whitlock, 1995) with the observed co-occurrence of Sitka spruce (*Picea sitchensis*) and subalpine fir (*Abies lasiocarpa*) from ca. 29.5 ka through 22.6 ka based on needle counts (Fig. 5; Marshall et al., 2015). These two species are rarely found together today at an elevation similar to Little Lake, with the exception of maritime cold parkland settings in SE Alaska (latitude 55.6°N) in a geographically restricted region near Hyder, Alaska (Thompson et al., 1999), and several nearby islands (Worley and Jaques, 1973). Additionally, we found pollen evidence of the lacustrine species *Nuphar* and *Potamogeton* throughout the core, which confirms sedimentological evidence of a deep-water setting, eliminating the need to consider nuclide inheritance in our sediments, as water would have rapidly attenuated cosmic rays.

Chronology and Depth-Age Model

We generated ages for the core intervals from plant macrofossils (radiocarbon) and sediments (OSL; Tables 1 and 2). The sediments preserve a high-fidelity record of past environments from 4 m below the surface to the original valley bottom. The radiocarbon dates suggest that the paleolake location changed from a depositional setting to intermittently erosional by ca. 20 ka.

We interpret the tephra deposits at 57 m and 56.5 m as aerial deposition followed by subsequent transport of hillslope-laid ash fall to the lake. Given that our depth-age curve suggests that the waterlain tephra deposit dates to 43.5 ka, and based on the tephra's distinct "salt-and-pepper" appearance, the deposit is likely the Mount St. Helens tephra set Cy (Ape Canyon Stage deposits). This initial eruptive stage spans 275–35 ka. It is divided into two distinct periods, 275–250 ka and 160–35 ka, with the C interval dated to ca. 50–35 ka (Clynne et al., 2008; Crandell, 1987; Kuehn and Negrini, 2010). Given the extensive Mount Mazama tephra deposits in the region, and more importantly the recovery of an ~1-cm-thick layer of Mount Mazama tephra deposits from the previous Little Lake core (Worona and Whitlock, 1995), we interpret the near-surface tephra deposits found in NOB A and NOB I as Mount Mazama (ca. 7.7 ka) in origin.

NOB I-P, at 3.22 m, dates to 21.6 ka and is only 0.29 m below NOB I-O, which contains the 7.7 ka Mount Mazama ash deposit (Fig. 5; Table 1). We used our near-surface ^{14}C dates to constrain the age of cosmogenic samples, as the bounding macrofossil samples are in chronological order. In Figure 5, we plot sample depth (below the surface) against age (yr B.P.) from 48.4 ka to 21.6 ka. Open triangles represent dates that we did not include in the depth-age model because they are anomalously old compared to neighboring samples and likely reflect reworked sediment with significant inheritance (Fig. 5; Table 1). Because the age-depth data have an inflection between 36 m (28 ka) and 41 m (30 ka) suggestive of two distinct depositional regimes, we plotted two separate linear regressions to estimate average sediment accumulation rates. This inflection point correlates with the observed major transition in vegetation types at 29 ka. Based on linear fits, the pre–27 ka sediment accumulation rates averaged 1 ± 0.003 mm yr^{-1}, and the 27–21 ka accumulation rates averaged 6 ± 0.085 mm yr^{-1}. Particularly notable is the >16.5 m of sediment dated between 24 ka and 23 ka (Table 1). While the three OSL samples have nontrivial errors, the dates are consistent with the ^{14}C dates, and thus we include them in the model (Fig. 4).

Temporal Variation of ^{10}Be Concentrations and Apparent Erosion Rates

We analyzed nuclide concentrations from 27 lacustrine samples and two modern samples collected from stream sediments above the paleolake influence (Fig. 1B). Using our CLAM depth-age model fit (Fig. 4) to assign ages to the CRN samples, we plotted ^{10}Be-derived apparent erosion rates against age (yr B.P.) in Figure 6. We report samples with very high errors (>2σ; Table 3), although we disregarded these samples in our evaluation of the results.

The ^{10}Be-derived (apparent) erosion rate at 46.4 ka is 0.06 ± 0.02 mm yr^{-1} and increases throughout MIS 3, concurrent with decreasing temperatures and a transition from temperate and montane forests to a subalpine parkland (Grigg et al., 2001; Worona and Whitlock, 1995). The erosion rate increase is not synchronous with the MIS 2 sediment accumulation rate increase (Fig. 4), but rather begins in MIS 3 (Fig. 6). By 28.5 ka, apparent erosion rates are 0.23 mm yr^{-1}, 3.8× greater than our oldest apparent erosion rate. Throughout MIS 2, erosion rates fluctuate around 0.21 ± 0.01 (mean ± SE) mm yr^{-1} (n = 7). Two clusters of samples at ca. 29 ka and ca. 25–23 ka have anomalously high ^{10}Be concentrations (and thus low apparent erosion

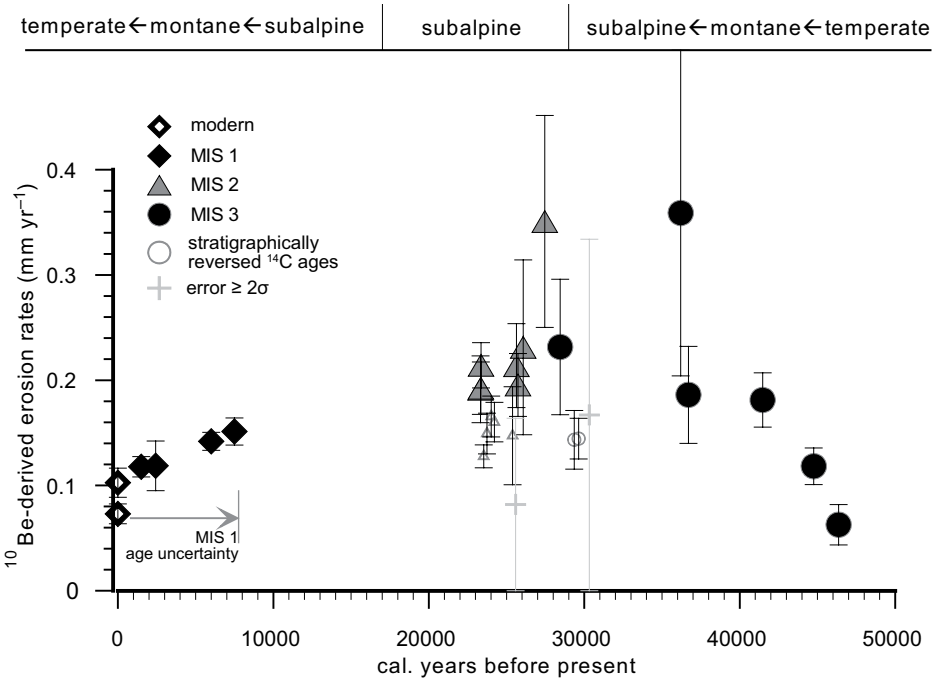

Figure 6. Little Lake ^{10}Be-derived erosion rates vs. time. All marine isotope stage (MIS) 1 samples are from lake sediments deposited above Mount Mazama tephra. As ages are unconstrained above the Mount Mazama tephra (ca. 7.6 ka) due to core incompleteness and inferred erosional episodes, we assigned approximate ages to the MIS 1 samples based on core chronology.

[1]GSA Data Repository item 2016362, figure describing complete macrofossil set identified in the Little Lake cores, is available at http://www.geosociety.org/pubs/ft2016.htm or by request to editing@geosociety.org.

rates). We discount these samples because they occur in the same period as age-reversed ^{14}C fossils (Figs. 4 and 5; see Discussion—Lake History), which indicate reworked sediment or mass movement of stored sediments. In addition, the abrupt erosion rate decreases implied by these samples is untenable over such a short time span (Fig. 3; see Discussion—Lake History) according to the systematics of cosmogenic nuclides. During the Holocene, as temperatures warmed and the ecosystem transitioned from montane to temperate forests, the apparent erosion rates decrease monotonically, with our sample from just above the 7.6 ka Mount Mazama ash yielding an erosion rate of 0.15 ± 0.01 mm yr^{-1} and modern samples averaging 0.08 ± 0.01 mm yr^{-1}.

Due to the transition to an intermittently nondepositional setting at our core site by ca. 20 ka, we have no samples that span the late glacial to early Holocene transition (the period between ca. 22.6 and 8 ka). Samples from NOB A2 and A4 cores have age constraints with significant uncertainty owing to imprecise depth control (see Results—Core Observations). We extracted the NOB A4 (3.33 m) sample from sediments deposited directly above the Mount Mazama tephra deposit, so we assign an age of 7.5 ka to the sample (Fig. 5). For sample A2 (2.54 m), we estimated an age of 6.0 ka, acknowledging that it could be younger. While we have a radiocarbon date of 2427 ± 25 yr for LIT I-L (2.17 m), we were unable to obtain radiocarbon dates from LIT I-D (1.15 m), ~1 m above LIT I-L, because we were unable to distinguish fossil material from modern surface plants with deep roots penetrating the paleodeposits. However, given that the LIT core data come from an active deposition area near the modern Little Lake (Fig. 1), we are confident that the sample underlies modern deposits and is younger than the 2.4 ka sample (LIT I-L), and thus we assign an age of 1500 (± 900) yr.

DISCUSSION

Our results suggest that climate change may have a profound influence on erosion rates. Apparent erosion rates at Little Lake track climate over nearly 50 k.y., with a 3.2× increase in apparent erosion rates coincident with declining temperatures, from the preglacial MIS 3 to the glacial MIS 2. Apparent LGM erosion rates are 2.5× higher than modern erosion rates (Figs. 4 and 6; Table 3). Our core data imply over 25 m of sediment accumulation over the span of the LGM, which implies exhumation and transport of nearly 5 m of sediment across the entire watershed during the LGM (Fig. 6; Table 1; Marshall et al., 2015). Next, we first use our high-resolution LiDAR data, core data, field observations, and the cosmogenic nuclide theoretical framework to assess likely sources for clusters of age-reversed fossil data that coincide with sediment samples with high ^{10}Be concentrations. Our interpretation of the coupling between hillslope sediments and the evolving landslide dam and lake levels leads to a potential explanation for the time lag between increasing erosion rates and increasing sediment accumulation in the watershed. In addition, we discuss hypothesized mechanisms for climate-induced changes in soil production, transport, and observed apparent erosion rates based on the paleoecological evidence and climate reconstructions and simulations. Finally, we use our transient erosion rate and mixing model to evaluate the range of potential actual erosion rates in the Little Lake watershed over the last 50 k.y.

Lake History—Nuclide Inheritance and Sediment Accumulation Conundrums

Our erosion rate data show an abrupt transition from 0.214 ± 0.04 mm yr^{-1} at 25,650 yr B.P. to 0.147 ± 0.07 mm yr^{-1} at 25,390 yr B.P. Just as abruptly, erosion rates return to 0.214 ± 0.02 mm yr^{-1} at 23, 360 yr B.P. Over the same interval where apparent erosion rates slow, the sediment accumulation rates at the core site rapidly increase. Given that CRN-derived erosion rates integrate concentrations over the length of cosmic-ray attenuation (~80 cm in the Little Lake watershed or ~2–4 k.y. depending on erosion rates), there is no feasible mechanism, with the exception of catchment-wide bedrock landslides, that could increase apparent nuclide concentrations in the integrated lake sediments by 1.5× over such a short interval of time (<400 yr; Fig. 3). However, the high-resolution bare earth LiDAR data show no evidence of significant bedrock landslide sources in the catchment.

Instead, we suggest that these rapid apparent erosion rate changes may be attributable to redeposition of marginal (or fan) sediments driven by dam breakouts and associated lake-lowering events. Additionally, we speculate that the increase in sediment accumulation rates during MIS 2 reflects a combination of remobilized lake-margin sediments, prograding deltas or fans, and an increase in sediment transport rates with the onset of the full glacial at 29 ka and the observed major vegetation transition.

Based on our LiDAR data and field observations, bench-cut terraces suggest that paleolake levels could have been as high as 290 masl compared to the present-day outlet connecting to Triangle Lake at 213 masl (Fig. 1). At a minimum, the lake elevation dropped from 260 masl to the broad spillway at 240 masl before cutting the lower-elevation outlet in the landslide deposit to the east-northeast of the former spillway (Fig. 1). Based on the combination of field evidence of thick fluvial gravels overlying the landslide deposit in the spillway with an elevation similar to that of the beveled landslide deposit and the cluster of both age-reversed fossils and high ^{10}Be concentrations starting at ca. 27 ka ± 1 ka, significant lowering events around ca. 27 ka and ca. 30 ka may contribute to our sedimentary record (Figs. 2 and 5; Tables 1 and 3). While we have no radiocarbon dates for the interval spanning 30,230 yr to 28,480 yr B.P., the samples exhibit a similar rapid rise and fall in apparent erosion rates. Given lake lowering, it is reasonable that sediment stored in steep alluvial fans or deltas along the lake margins would have been remobilized. Other substantial opportunities for significant sediment storage are sparse; hillslope gradients that average 70% are connected by narrow valleys. In addition, observable alluvial fans and dissected backwater deposits in the lake-bounding tributaries in the Little Lake LiDAR data (Fig. 1A; Marshall et al., 2016) are consistent with our interpretation.

Due to the unusually high uncertainties in some of our samples (Table 3), there is potential overlap between these two "populations" of CRN-derived erosion rates; however, the high-concentration values are both systematically lower than the bracketing erosion rates and cluster in narrow age ranges, which suggest random uncertainty is unlikely to be the source of the observed concentration excursions. During sample preparation, we carefully avoided apparent landslide deposits when selecting samples from the extensive coarse-sand–sized MIS 2 deposits. Therefore, we do not favor (but cannot eliminate) the alternative interpretation that the low-concentration samples derive from shallow landslides, and that the observed high concentration data are reflective of colluvial processes.

Climate-Mediated Changes in Soil Production Mechanisms

In Little Lake, apparent erosion rates declined coincident with the transition from a subalpine setting to the modern temperate climate (Grigg et al., 2001; Worona and Whitlock, 1995). Schaller et al. (2002) reported a similar decline in erosion rates from the LGM to present in an unglaciated basin with apparent erosion rates at 20 ka 2.7× higher than modern catchment-derived erosion rates. They suggested that higher erosion rates correlate with a periglacial setting during glacial intervals as recorded in marine isotope data. At our Little Lake study area, we tested this idea via a suite of paleoclimate reconstructions and models, presented next, in conjunction with our apparent erosion rate time

series. These process models and paleoclimate reconstructions provide support for the role of periglacial processes in the acceleration of soil production, transport, and erosion rates leading up to MIS 2 at Little Lake.

Frost Weathering Model

Given the cold and dry climate inferred for 29.5 ka at Little Lake (Fig. 5; supplemental material [see footnote 1]), which suggests a modern southeast Alaska analog climate, we modeled frost weathering intensity at Little Lake based on paleotemperature data (Marshall et al., 2015). Bedrock fracturing occurs when ice lenses grow in rock pore spaces at temperatures between approximately –3 °C and –8 °C (Anderson, 1998; Hales and Roering, 2007; Walder and Hallet, 1985). Frost damage is controlled by water availability, mean annual temperatures (MAT), and annual temperature amplitudes (Anderson et al., 2013; Hales and Roering, 2007).

Our model quantifies the intensity of frost weathering as a linear function of the depth-integrated temperature gradient. We defined the frost-weathering index as the annual integral of the depth-integrated daily temperature gradient (°C-day) for substrate within the –3 °C and –8 °C temperature range. While MAT at modern Little Lake is ~11 °C, with an amplitude of ~7 °C, MAT at Little Lake ca. 21 ka was ~0 °C with an amplitude of ~8 °C (Fig. 7).

According to our model, the amplitude of seasonal temperature variation and MAT are the dominant factors controlling the vigor of frost weathering. Thus, we used a contour plot of frost weathering intensity as a function of amplitude and MAT to predict how frost weathering intensity might have increased through time at Little Lake. Our Little Lake paleoclimate reconstruction allows us to infer MAT throughout MIS 3 and 2 to calculate frost cracking intensity. Little Lake pollen data suggest an overall cooling trend and subalpine conditions occurring in >50% of the recorded climate interval (Grigg et al., 2001; Fig. 5). By 27.8 ka, Little Lake was a subalpine parkland meadow setting. These climatic conditions persisted throughout the glacial interval. As MAT variations increase during glacial intervals due to differences in summer insolation and the degree of ocean and land surface interactions (French, 2013), we approximated the transition from the paleoclimate amplitude at 21 ka to the modern Little Lake climate amplitude. For this transition, we plotted frost cracking intensity based on inferred temperatures for the dominant LL-1 pollen subzones (Fig. 8).

At 42.7 ka (LL-1a), pollen suggests a hemlock pine forest, with temperatures cooler than present. Grigg et al. (2001) did not infer a MAT for this pollen zone. However, on a plot of inferred climate for MIS 3 and 2, they assigned this zone the warmest temperatures of any Little Lake pollen subzone. Additionally, the LL-1a forest type is similar to western Vancouver Island, with abundant cedar and hemlock, minimal Douglas fir, and some western pine, where January temperatures average ~4 °C, MAT is ~7 °C, and it rarely snows (ClimateWNA, 2016). We therefore assume that temperatures would have allowed for minor excursions into the frost-cracking window. As temperatures cooled and amplitudes modestly increased, frost weathering intensity would have increased, concurrent with the apparent increase in erosion rates (Fig. 6). Even during periods when the montane forests returned, January and February temperatures were likely low enough to generate frost weathering over short periods, increasing rock weathering and priming the substrate for future disruption.

Forests and Frost: Climate Transitions and Soil Production Mechanisms

Given the likelihood of frost weathering based on our paleoclimate reconstruction and simulations (Figs. 7 and 8), a profound shift in sediment character, increases in grain size, angularity, and lamination spacing (Fig. 5), a 6× increase in sediment accumulation rates (Fig. 4), an increase in apparent erosion rates concurrent with climate cooling during MIS 3, and MIS 2 apparent erosion rates 2.5× greater than modern MIS 1 erosion rates (Fig. 6), we hypothesize

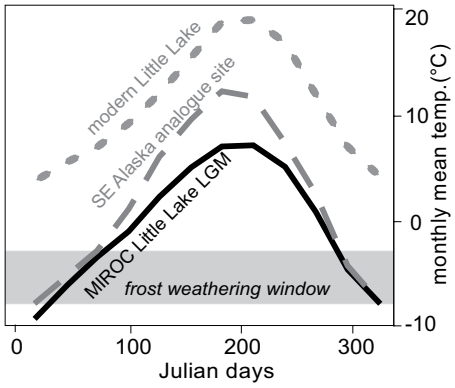

Figure 7. Comparison of annual temperature curves based on: mean monthly temperature data for modern Little Lake (short dashed gray line), modern data from a representative Last Glacial Maximum (LGM) analogue location near Hyder, Alaska (long dashed gray line), and downscaled paleoclimate simulation data from earth system model MIROC-ESM (solid black line). Figure is modified from Marshall et al. (2015).

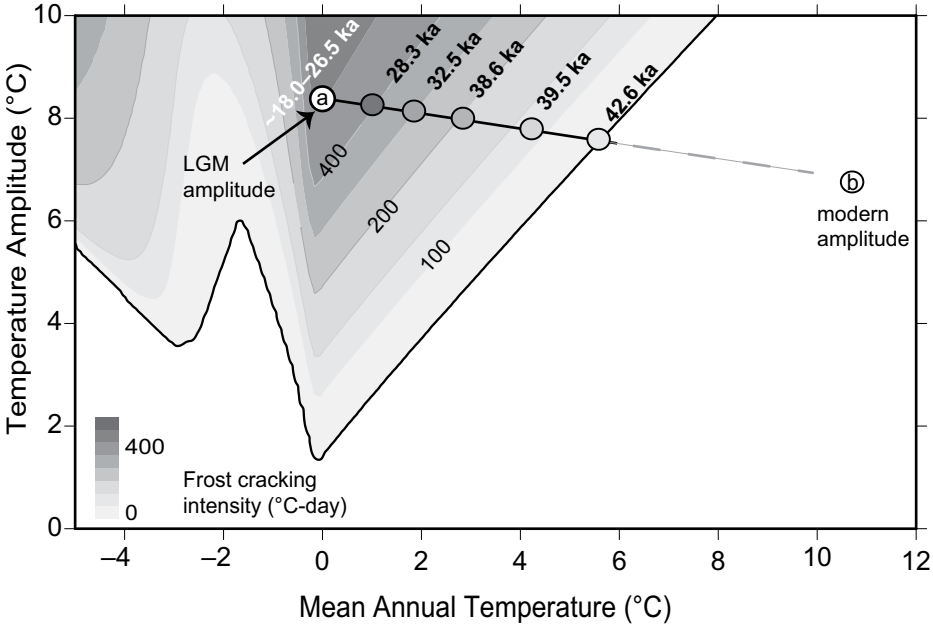

Figure 8. Frost-cracking intensity and paleoclimate reconstructions. Mean annual temperature (MAT) and amplitude values for Little Lake at 21 ka and the present, marked by "a" and "b," respectively. Line represents change in annual temperature amplitude from glacial to interglacial intervals. Circles are frost-cracking intensity at Little Lake for marine isotope stage (MIS) 3 and MIS 2 pollen zone intervals based on inferred Little Lake temperatures (Grigg et al., 2001), core fossil data, and Last Glacial Maximum (LGM) paleoclimate simulations (Marshall et al., 2015). Figure is modified from Marshall et al. (2015).

that frost processes (e.g., frost cracking, heave, creep, and solifluction) increasingly dominated bedrock weathering, soil production, transport, and erosion during the late stages of MIS 3 and throughout the glacial MIS 2. As cosmogenic-derived erosion rates integrate information over thousands of years (Fig. 3), the persistence of high erosion rates during the LGM implies that soil production rates increased before the onset of the glacial interval.

During warm, forested climate intervals (e.g., MIS 1 and 3), bedrock damage and detachment via tree roots can range from cantilever-like leverage exerted by large-diameter trees during windstorms (Lutz, 1960) to simple displacement via lift forces generated by roots extending along horizontal bedding planes (Marshall and Roering, 2014). Given the low basal area of mature Douglas fir trees (~1%; Tappeiner et al., 1997), bedrock to soil conversion and the initiation of disrupted regolith for transport via trees are stochastic both spatially and temporally.

In contrast to stochastic tree-driven hillslope processes observed during MIS 1 and thus likely during MIS 3, frost-controlled soil production may have been spatially pervasive at Little Lake starting with cold excursions in MIS 3 and throughout MIS 2. Given the small range in elevation of 200–500 m in the 6 km^2 watershed, altitudinal temperature variation is negligible, suggesting minor variation in temperature-controlled processes. During the LGM, frost damage would have occurred in both the winter and spring months (Grigg et al., 2001) and frost damage likely extended up to 2–4 m below the surface (Hales and Roering, 2007; Rempel et al., 2016).

Whereas frost weathering damages rock, frost heave, particularly active at temperatures of ~0 °C (Matsuoka, 2001), is efficient at transporting sediment downslope (Saunders and Young, 1983), such that hillslopes were unlikely to be transport limited. The Little Lake hillslope gradients are steep (0.70 ± 0.2, mean ± SD) and narrow, with confined valley bottoms, implying rapid sediment transport and minimal opportunity for storage. The mechanics and efficiency of frost heave, needle ice creep, frost creep, plug-like flow, etc., are dependent on a range of factors, including one- versus two-sided freezing, freeze-thaw cycle frequency, moisture availability, and frost susceptibility of the soil (French, 2013; Harris et al., 2008; Matsuoka, 2001; Smith, 1992). Nonetheless, hillslope gradient is a first-order control on soil transport (French, 2013), and mean solifluction rates in steep montane topography average ~6 cm yr^{-1}, compared to soil creep rates of ~1 cm yr^{-1} in forested, temperate settings (Matsuoka, 2001; Saunders and Young, 1983). In modern settings with steep slopes, seasonal frost, and MAT similar to Little Lake's LGM MAT of ~0 °C, solifluction rates approach ~20 cm yr^{-1} (Matsuoka, 2001). In addition, given the 76 cm cosmic-ray attenuation depth, LGM regolith production must have been rapid in order to accommodate the sustained delivery of low-concentration samples observed in our core. While modern estimated OCR maximum soil production rates approach 0.27 mm yr^{-1} as soil depths approach zero (Heimsath et al., 2001), it is unlikely that the soil production estimated for the Holocene ecosystem has relevance for interpreting soil production during the LGM. Therefore, we expect that frost-driven soil production and transport rates at Little Lake exceeded biogenic-driven rates, which would account for the observed LGM increase in erosion rates.

Theoretical Model for Apparent versus Actual Erosion Rates

We used our transient paleo-erosion model to interpret how changes in erosion rates and mixing depths might influence ^{10}Be concentrations at our Little Lake site (Fig. 9). A priori knowledge of apparent ^{10}Be-derived erosion rates informed our model, while the pollen records informed our choice of erosion rate time intervals. We chose mixing depths that were consistent with rooting data inferred from the paleoenvironmental record, inferred LGM periglacial conditions, and the modern ecosystem. For computational simplicity, we only considered nuclide production due to spallation. This simplification results in apparent erosion rates that are ~9% lower than if we incorporated

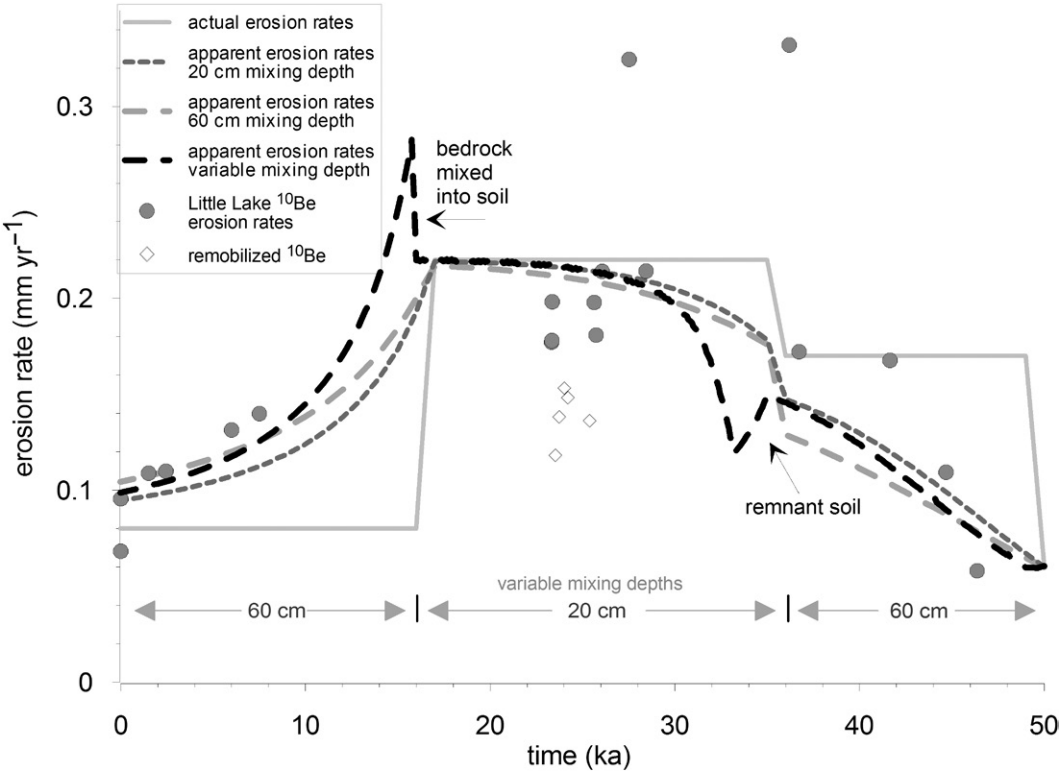

Figure 9. Transient mixing depths and erosion rate model output compared to Little Lake ^{10}Be-derived erosion rates. Solid line delineates modeled actual erosion rates; dashed lines delineate model results for apparent erosion rates with diverse soil mixing scenarios. Model output with variable mixing depths has depths noted at each of the three time intervals.

muon production, but the relative erosion rate differences documented here are robust.

In this exploratory exercise, we started the model at 50 ka with an erosion rate of 0.06 mm yr^{-1} and imposed an increase to 0.17 mm yr^{-1} at 49 ka. Given steadily increasing apparent erosion rates at Little Lake during MIS 3 (Fig. 6) and the asymptotic nature of apparent transient erosion rates (Fig. 3), it is reasonable to expect that erosion rates were already increasing at or before 49 ka. At 35 ka, when temperatures were cold enough for frost process conditions to be prevalent (Fig. 8; Grigg et al., 2001), we imposed a new erosion rate of 0.22 mm yr^{-1}. At 16 ka, as the glacial interval was waning and mesic forests were establishing (Grigg et al., 2001; Worona and Whitlock, 1995), we imposed an erosion rate of 0.08 mm yr^{-1}, as environmental conditions 16 ka are similar to those recorded in modern Little Lake sediments.

In the simulation, we explored how constant mixing depths of 20 and 60 cm differ from varying mixing depths (Fig. 9). Given modern forest soil depths in the OCR (Heimsath et al., 2001; Reneau and Dietrich, 1991; Roering et al., 2010), we assigned a mixing depth of 60 cm to the forested intervals (MIS 3 and 1). During the subalpine environment (late MIS 3 and MIS 2), we speculated that frost heave would have controlled mixing depths, and we assigned a mixing depth of 20 cm, based on measured diurnal frost penetration depths from sites with seasonal frost and MAT ~ 0 °C (Matsuoka, 2001).

Our model results show that the deeper the mixing depth, the greater is the lag between actual and apparent erosion rates. Additionally, our modeled apparent erosion rates reflect transient excursions in apparent erosion rates as climate-driven processes likely shift mixing depths and actual erosion rates. Absent rigorous simulation and parameter optimization, these findings, which use reasonable mechanistic assumptions based on the paleoenvironmental reconstructions, and a priori knowledge of the minimum erosion rates from our ^{10}Be-derived erosion rates, agree well with apparent erosion rates at Little Lake, although alternative erosion rate histories may prove reasonable. Additionally, our model output (and Eq. 2) suggests that without paleo-erosion data between the late Pleistocene and the early to mid-Holocene (Fig. 5; Table 1), we are unable to conclude that modern apparent erosion rates have equilibrated to actual erosion rates.

CONCLUSIONS

By coupling diverse tools and analyses, including a frost weathering model, sedimentology, paleoecology, and isotopic-derived paleoerosion data from a new sediment archive extracted from a 50 ka paleolake deposit, we propose that climate modulated erosion rates over glacial-interglacial time scales at our western Oregon study area. The ^{10}Be-derived erosion rates more than tripled as the unglaciated OCR transitioned from the forested MIS 3 pre-LGM climate interval into the periglacial subalpine MIS 2 glacial interval. Then, apparent erosion rates declined by more than half as the LGM subalpine ecosystem transitioned to the modern MIS 1 Douglas fir forest. Our findings challenge the notion that modern processes in unglaciated midlatitude terrain can be projected into the past beyond the current interglacial interval. In addition, our cosmogenic nuclide data and model results suggest caution when assuming steady erosion to interpret the balance of tectonic forcing and denudation, as changes in mixing depths risk being interpreted as sudden changes in uplift rates or base level.

In our Oregon Coast Range setting, our data are consistent with abiotic frost processes driving accelerated erosion such that apparent erosion rates during the LGM were 2.8× faster than modern rates. Additionally, with the transition from a forested to subalpine parkland setting, lake sediment accumulation rates increased by up to a factor of 6 during the LGM. While frost-driven processes likely increased sediment production and transport rates and thus fluxes, our core may also incorporate punctuated deposits that originated from remobilized marginal sediments. By employing a transient framework that incorporates changing mixing depths and erosion rates for assessing nuclide inventories in a soil column, we established the importance of considering process-driven changes in soil mixing depths when evaluating apparent erosion rates. Our model results suggest that actual LGM erosion rates, driven by frost processes, may have been up to 4× faster than tree-driven erosion rates associated with more temperate climes.

Our findings encourage a reevaluation of what constitutes steady state in soil-mantled unglaciated settings. Importantly, cold intervals with vigorous frost activity may be the primary pacesetters of landscape evolution in unglaciated terrain.

ACKNOWLEDGMENTS

This research was funded by a National Science Foundation (NSF) grant, Geomorphology and Land Use Dynamics, EAR- 0952186. We thank Aurelie and Jim Noble for drilling and sampling access on their property and their generous support of scientific discovery. Erin Herring, Corina Cerovski-Darriau, and Hannah Grist provided invaluable assistance in both the field and laboratory. Helpful comments from Science Editor Aaron Cavosie and Associate Editor Ben Laabs, and reviews from two anonymous reviewers significantly improved the manuscript.

REFERENCES CITED

Ahnert, F., 1994, Equilibrium, scale and inheritance in geomorphology: Geomorphology, v. 11, p. 125–140, doi:10.1016/0169-555X(94)90077-9.

Almond, P., Roering, J., and Hales, T.C., 2007, Using soil residence time to delineate spatial and temporal patterns of transient landscape response: Journal of Geophysical Research, v. 112, p. F03S17, doi:10.1029/2006JF000568.

Anderson, R.S., 1998, Near-surface thermal profiles in alpine bedrock: Implications for the frost weathering of rock: Arctic and Alpine Research, v. 30, p. 362–372, doi:10.2307/1552008.

Anderson, R.S., Anderson, S.P., and Tucker, G.E., 2013, Rock damage and regolith transport by frost: An example of climate modulation of the geomorphology of the critical zone: Earth Surface Processes and Landforms, v. 38, p. 299–316, doi:10.1002/esp.3330.

Anderson, S.P., Dietrich, W.E., and Brimhall, G.H., 2002, Weathering profiles, mass-balance analysis, and rates of solute loss: Linkages between weathering and erosion in a small, steep catchment: Geological Society of America Bulletin, v. 114, p. 1143–1158, doi:10.1130/0016-7606(2002)114<1143.

Balco, G., Stone, J.O., Lifton, N.A., and Dunai, T.J., 2008, A complete and easily accessible means of calculating surface exposure ages or erosion rates from ^{10}Be and ^{26}Al measurements: Quaternary Geochronology, v. 3, p. 174–195, doi:10.1016/j.quageo.2007.12.001.

Balco, G., Finnegan, N., Gendaszek, A., Stone, J.O.H., and Thompson, N., 2013, Erosional response to northward-propagating crustal thickening in the coastal ranges of the U.S. Pacific Northwest: American Journal of Science, v. 313, p. 790–806, doi:10.2475/11.2013.01.

Barry, R.G., 1998, Palaeoclimatology, climate system processes and the geomorphic record, *in* Stoddart, D., ed., Process and Form in Geomorphology: London, New York, Routledge, p. 187–214.

Bekaddour, T., Schlunegger, F., Vogel, H., Delunel, R., Norton, K.P., Akçar, N., and Kubik, P., 2014, Paleo erosion rates and climate shifts recorded by Quaternary cut-and-fill sequences in the Pisco valley, central Peru: Earth and Planetary Science Letters, v. 390, p. 103–115, doi:10.1016/j.epsl.2013.12.048.

Bierman, P., Clapp, E., Nichols, K., Gillespie, A., and Caffee, M., 2001, Using cosmogenic nuclide measurements in sediments to understand background rates of erosion and sediment transport, *in* Harmon, R.S., and Doe, W.W., III, eds., Landscape Erosion and Evolution Modelling: New York, Kluwer, p. 89–115, doi:10.1007/978-1-4615-0575-4_5.

Blaauw, M., 2010, Methods and code for "classical" age-modelling of radiocarbon sequences: Quaternary Geochronology, v. 5, p. 512–518, doi:10.1016/j.quageo.2010.01.002.

Blechschmidt, I., Matter, A., Preusser, F., and Rieke-Zapp, D., 2009, Monsoon triggered formation of Quaternary alluvial megafans in the interior of Oman: Geomorphology, v. 110, p. 128–139, doi:10.1016/j.geomorph.2009.04.002.

Borchers, B., Marrero, S., Balco, G., Caffee, M., Goehring, B., Lifton, N., Nishiizumi, K., Phillips, F., Schaefer, J., and Stone, J., 2016, Geological calibration of spallation production rates in the CRONUS-Earth project: Quaternary Geochronology, v. 31, p. 188–198, doi:10.1016/j.quageo.2015.01.009.

Brocklehurst, S.H., and Whipple, K.X., 2002, Glacial erosion and relief production in the Eastern Sierra Nevada, California: Geomorphology, v. 42, p. 1–24, doi:10.1016/S0169-555X(01)00069-1.

Bull, W., 1991, Geomorphic Responses to Climatic Change: New York, Oxford University Press, 325 p.

Chan, M.A., and Dott, R.H.J., 1986, Depositional facies and progradational sequences in Eocene wave-dominated deltaic complexes, southwestern Oregon: American Association of Petroleum Geologists Bulletin, v. 70, no. 4, p. 415–429.

Charreau, J., Blard, P.-H., Puchol, N., Avouac, J.-P., Lallier-Vergès, E., Bourlès, D., Braucher, R., Gallaud, A., Finkel, R., Jolivet, M., Chen, Y., and Roy, P., 2011, Paleo-erosion rates in Central Asia since 9 Ma: A tran-

sient increase at the onset of Quaternary glaciations?: Earth and Planetary Science Letters, v. 304, p. 85–92, doi:10.1016/j.epsl.2011.01.018.

Chorley, R.J., Schumm, S.A., and Sugden, D.E., 1984, Geomorphology: New York, Methuen & Co, 605 p.

Church, M., and Ryder, J.M., 1972, Paraglacial sedimentation: A consideration of fluvial processes conditioned by glaciation: Geological Society of America Bulletin, v. 83, p. 3059–3072, doi:10.1130/0016-7606(1972)83[3059:PSACOF]2.0.CO;2.

ClimateWNA, 2016, ClimateWNA: University of British Columbia, http://climatewna.com/ (last accessed 7 January 2016).

Clynne, M.A., Calvert, A.T., Wolfe, E.W., Evarts, R.C., Fleck, R.J., and Lanphere, M.A., 2008, The Pleistocene eruptive history of Mount St. Helens, Washington, from 300,000 to 12,800 years before present, *in* Sherrod, D.R., Scott, W.E., and Stauffer, P.H., eds., A Volcano Rekindled: The Renewed Eruption of Mount St. Helens, 2004–2006: U.S. Geological Survey Professional Paper, p. 593–627.

Crandell, D.R., 1987, Deposits of Pre-1980 Pyroclastic Flows and Lahars from Mount St. Helens Volcano: U.S. Geological Survey Professional Paper 1444, 102 p., http://pubs.usgs.gov/pp/1444/report.pdf.

Delunel, R., van der Beek, P.A., Carcaillet, J., Bourlès, D.L., and Valla, P.G., 2010, Frost-cracking control on catchment denudation rates: Insights from in situ produced ^{10}Be concentrations in stream sediments (Ecrins–Pelvoux massif, French Western Alps): Earth and Planetary Science Letters, v. 293, p. 72–83, doi:10.1016/j.epsl.2010.02.020.

Dietrich, W.E., and Dunne, T., 1978, Sediment budget for a small catchment in mountainous terrain: Zeitschrift für Geomorphologie N.F., v. 29, p. 191–206, doi:10.1007/s10069-002-0008-0.

Dietrich, W.E., and Perron, J.T., 2006, The search for a topographic signature of life: Nature, v. 439, p. 411–418, doi:10.1038/nature04452.

Dietrich, W.E., Bellugi, D.G., Sklar, L.S., Stock, J.D., Heimsath, A.M., and Roering, J.J., 2003, Geomorphic transport laws for predicting landscape form and dynamics, *in* Wilcock, P.R., and Iverson, R.M., eds., Predictions in Geomorphology: American Geophysical Union Geophysical Monograph 135, p. 103–132, doi:10.1029/135GM09.

Dunwiddie, P.W., 1985, Dichotomous key to conifer foliage in the Pacific Northwest: Northwest Science, v. 59, p. 185–191.

French, H.M., 2013, The periglacial environment: Chichester, UK, John Wiley & Sons, 458 p.

Granger, D.E., and Muzikar, P.F., 2001, Dating sediment burial with in situ–produced cosmogenic nuclides: Theory, techniques, and limitations: Earth and Planetary Science Letters, v. 188, p. 269–281, doi:10.1016/S0012-821X(01)00309-0.

Granger, D.E., and Riebe, C.S., 2014, Cosmogenic nuclides in weathering and erosion, *in* Drever, J.I., ed., Treatise on Geochemistry: London, Elsevier, p. 401–436, doi:10.1016/B978-0-08-095975-7.00514-3.

Granger, D.E., and Schaller, M., 2014, Cosmogenic nuclides and erosion at the watershed scale: Elements, v. 10, p. 369–373, doi:10.2113/gselements.10.5.369.

Granger, D.E., Kirchner, J.W., and Finkel, R., 1996, Spatially averaged long-term erosion rates measured from in situ–produced cosmogenic nuclides in alluvial sediment: The Journal of Geology, v. 104, p. 249–257, doi:10.1086/629823.

Grigg, L.D., and Whitlock, C., 1998, Late-glacial vegetation and climate change in western Oregon: Quaternary Research, v. 49, p. 287–298, doi:10.1006/qres.1998.1966.

Grigg, L.D., and Whitlock, C., 2002, Patterns and causes of millennial-scale climate change in the Pacific Northwest during marine isotope stages 2 and 3: Quaternary Science Reviews, v. 21, p. 2067–2083, doi:10.1016/S0277-3791(02)00017-3.

Grigg, L.D., Whitlock, C., and Dean, W.E., 2001, Evidence for millennial-scale climate change during marine isotope stages 2 and 3 at Little Lake, western Oregon, U.S.A.: Quaternary Research, v. 56, p. 10–22, doi:10.1006/qres.2001.2246.

Hack, J.T., 1975, Dynamic equilibrium and landscape evolution, *in* Melhorn, W.N., and Flemal, R.C., eds., Theories of Landform Development, Volume 1: London, George Allen & Unwin, p. 87–102.

Hales, T.C., and Roering, J.J., 2007, Climatic controls on frost cracking and implications for the evolution of bedrock landscapes: Journal of Geophysical Research, v. 112, p. F02033, doi:10.1029/2006JF000616.

Harris, C., Kern-Luetschg, M., Murton, J., Font, M., Davies, M., and Smith, F., 2008, Solifluction processes on permafrost and non-permafrost slopes: Results of a large-scale laboratory simulation: Permafrost and Periglacial Processes, v. 19, p. 359–378, doi:10.1002/ppp.630.

Heimsath, A.M., 2006, Eroding the land: Steady-state and stochastic rates and processes through a cosmogenic lens, *in* Alonso-Zarza, A.M., and Tanner, L.H., eds., In Situ–Produced Cosmogenic Nuclides and Quantification of Geological Processes: Geological Society of America Special Paper 415, p. 111–129.

Heimsath, A.M., Dietrich, W.E., Nishiizumi, K., and Finkel, R.C., 2001, Stochastic processes of soil production and transport: Erosion rates, topographic variation and cosmogenic nuclides in the Oregon Coast Range: Earth Surface Processes and Landforms, v. 26, p. 531–552, doi:10.1002/esp.209.

Heller, P.L., and Dickinson, W.R., 1985, Submarine ramp facies model for delta-fed, sand-rich turbidite systems: American Association of Petroleum Geologists Bulletin, v. 69, p. 960.

Herman, F., and Braun, J., 2008, Evolution of the glacial landscape of the Southern Alps of New Zealand: Insights from a glacial erosion model: Journal of Geophysical Research, v. 113, p. F02009, doi:10.1029/2007JF000807.

Herman, F., Seward, D., Valla, P.G., Carter, A., Kohn, B., Willett, S.D., and Ehlers, T.A., 2013, Worldwide acceleration of mountain erosion under a cooling climate: Nature, v. 504, p. 423–426, doi:10.1038/nature12877.

Hidy, A.J., Gosse, J.C., Blum, M.D., and Gibling, M.R., 2014, Glacial–interglacial variation in denudation rates from interior Texas, USA, established with cosmogenic nuclides: Earth and Planetary Science Letters, v. 390, p. 209–221, doi:10.1016/j.epsl.2014.01.011.

Jerolmack, D.J., and Paola, C., 2010, Shredding of environmental signals by sediment transport: Geophysical Research Letters, v. 37, p. L19401, doi:10.1029/2010GL044638.

Kelsey, H.M., Ticknor, R.L., Bockheim, J.G., and Mitchell, E., 1996, Quaternary upper plate deformation in coastal Oregon: Geological Society of America Bulletin, v. 108, p. 843–860, doi:10.1130/0016-7606(1996)108<0843:QUPDIC>2.3.CO;2.

Kohl, C., and Nishiizumi, K., 1992, Chemical isolation of quartz for measurement of in-situ–produced cosmogenic nuclides: Geochimica et Cosmochimica Acta, v. 56, p. 3583–3587, doi:10.1016/0016-7037(92)90401-4.

Kuehn, S.C., and Negrini, R.M., 2010, A 250 k.y. record of Cascade arc pyroclastic volcanism from late Pleistocene lacustrine sediments near Summer Lake, Oregon, USA: Geosphere, v. 6, p. 397–429, doi:10.1130/GES00515.1.

Lal, D., 1991, Cosmic ray labeling of erosion surfaces: In situ nuclide production rates and erosion models: Earth and Planetary Science Letters, v. 104, p. 424–439, doi:10.1016/0012-821X(91)90220-C.

Lifton, Z.M., Thackray, G.D., Van Kirk, R., and Glenn, N.F., 2009, Influence of rock strength on the valley morphometry of Big Creek, central Idaho, USA: Geomorphology, v. 111, p. 173–181, doi:10.1016/j.geomorph.2009.04.014.

Lisiecki, L.E., and Raymo, M.E., 2005, A Pliocene-Pleistocene stack of 57 globally distributed benthic δ^{18}O records: Paleoceanography, v. 20, p. PA1003, doi:10.1029/2004PA001071.

Lutz, H., 1960, Movement of rocks by uprooting of forest trees: American Journal of Science, v. 258, p. 752–756, doi:10.2475/ajs.258.10.752.

Marshall, J.A., and Roering, J.J., 2014, Diagenetic variation in the Oregon Coast Range: Implications for rock strength, soil production, hillslope form, and landscape evolution: Journal of Geophysical Research–Earth Surface, v. 119, p. 1395–1417, doi:10.1002/2013JF003004.

Marshall, J.A., Cerovski-Darriau, C., and Roering, J.J., 2016, Smoothed LiDAR-derived bare-earth DEM and gradient geotiffs, Little Lake, OR, USA, doi:10.6084/m9.figshare.3545114.v2 (https://figshare.com/articles/Smoothed_lidar-derived_bare-earth_DEM_and_gradient_geotiffs_Little_Lake_OR_USA/3545114).

Marshall, J.A., Roering, J.J., Bartlein, P.J., Gavin, D.G., Granger, D.E., Rempel, A.W., Praskievicz, S.J., and Hales, T.C., 2015, Frost for the trees: Did climate increase erosion in unglaciated landscapes during the late Pleistocene?: Science Advances, v. 1, no. 10, doi:10.1126/sciadv.1500715.

Matsuoka, N., 2001, Solifluction rates, processes and landforms: A global review: Earth-Science Reviews, v. 55, p. 107–134, doi:10.1016/S0012-8252(01)00057-5.

McPhillips, D., Bierman, P.R., Crocker, T., and Rood, D.H., 2013, Landscape response to Pleistocene-Holocene precipitation change in the Western Cordillera, Peru: ^{10}Be concentrations in modern sediments and terrace fills: Journal of Geophysical Research–Earth Surface, v. 118, p. 2488–2499, doi:10.1002/2013JF002837.

Molnar, P., 2004, Late Cenozoic increase in accumulation rates of terrestrial sediment: How might climate change have affected erosion rates?: Annual Review of Earth and Planetary Sciences, v. 32, p. 67–89, doi:10.1146/annurev.earth.32.091003.143456.

Montgomery, D.R., 2001, Slope distributions, threshold hillslopes, and steady-state topography: American Journal of Science, v. 301, p. 432–454, doi:10.2475/ajs.301.4-5.432.

Montgomery, D.R., 2002, Valley formation by fluvial and glacial erosion: Geology, v. 30, p. 1047–1050, doi:10.1130/0091-7613(2002)030<1047:VFBFAG>2.0.CO;2.

Murray, A.S., and Wintle, A.G., 2003, The single aliquot regenerative dose protocol: potential for improvements in reliability: Radiation Measurements, v. 37, p. 377–381, doi:10.1016/S1350-4487(03)00053-2.

National Research Council (U.S.), 2010, Committee on Challenges and Opportunities in Earth Surface Processes; Landscapes on the Edge: New Horizons for Research on Earth's Surface: Washington, D.C., The National Academies Press, 180 p.

Niemi, N.A., Oskin, M., Burbank, D.W., Heimsath, A.M., and Gabet, E.J., 2005, Effects of bedrock landslides on cosmogenically determined erosion rates: Earth and Planetary Science Letters, v. 237, p. 480–498, doi:10.1016/j.epsl.2005.07.009.

Nishiizumi, K., Imamura, M., Caffee, M.W., Southon, J.R., Finkel, R.C., and McAninch, J., 2007, Absolute calibration of ^{10}Be AMS standards: Nuclear Instruments & Methods in Physics Research, Section B, Beam Interactions with Materials and Atoms, v. 258, p. 403–413, doi:10.1016/j.nimb.2007.01.297.

Oregon Water Resource Department, 2014, Well log data: http://apps.wrd.state.or.us/apps/gw/well_log/Default.aspx (last accessed 12 March 2014).

Orr, E., Orr, W., and Baldwin, E., 1992, Geology of Oregon: Dubuque, Iowa, Kendall/Hunt Publishing Company, 254 p.

Pederson, J., Smith, G., and Pazzaglia, F., 2001, Comparing the modern, Quaternary, and Neogene records of climate-controlled hillslope sedimentation in southeast Nevada: Geological Society of America Bulletin, v. 113, p. 305–319, doi:10.1130/0016-7606(2001)113<0305:CTMQAN>2.0.CO;2.

PRISM Climate Group, 2010, PRISM Climate Group: Oregon State University, http://www.prismclimate.org (created 12 March 2010).

PRISM Climate Group, 2016, PRISM Climate Group: Oregon State University, http://prism.oregonstate.edu (created 25 July 2016).

Refsnider, K.A., 2010, Dramatic increase in late Cenozoic alpine erosion rates recorded by cave sediment in the southern Rocky Mountains: Earth and Planetary Science Letters, v. 297, p. 505–511, doi:10.1016/j.epsl.2010.07.002.

Reimer, P., Bard, E., Bayliss, A., et al., 2013, IntCal13 and Marine13 radiocarbon age calibration curves 0–50,000 Years cal BP: Radiocarbon, v. 55, p. 1869–1887, doi:10.2458/azu_js_rc.55.16947.

Rempel, A.W., Marshall, J.A., and Roering, J.J., 2016, Modeling relative frost weathering rates at geomorphic

scales: Earth and Planetary Science Letters, v. 453, p. 87–95, doi:10.1016/j.epsl.2016.08.019.

Reneau, S.L., and Dietrich, W.E., 1991, Erosion rates in the southern Oregon Coast Range: Evidence for an equilibrium between hillslope erosion and sediment yield: Earth Surface Processes and Landforms, v. 16, p. 307–322, doi:10.1002/esp.3290160405.

Riebe, C.S., Kirchner, J.W., Granger, D.E., and Finkel, R.C., 2001a, Minimal climatic control on erosion rates in the Sierra Nevada, California: Geology, v. 29, p. 447–450, doi:10.1130/0091-7613(2001)029<0447:MCCOER>2.0.CO;2.

Riebe, C.S., Kirchner, J.W., Granger, D.E., and Finkel, R.C., 2001b, Strong tectonic and weak climatic control of long-term chemical weathering rates: Geology, v. 29, p. 511–514, doi:10.1130/0091-7613(2001)029<0511:STAWCC>2.0.CO;2.

Riebe, C.S., Kirchner, J.W., and Granger, D.E., 2001c, Quantifying quartz enrichment and its consequences for cosmogenic measurements of erosion rates from alluvial sediment and regolith: Geomorphology, v. 40, p. 15–19, doi:10.1016/S0169-555X(01)00031-9.

Roering, J.J., Kirchner, J.W., and Dietrich, W.E., 1999, Evidence for nonlinear, diffusive sediment transport on hillslopes and implications for landscape morphology: Water Resources Research, v. 35, p. 853–870, doi:10.1029/1998WR900090.

Roering, J.J., Kirchner, J.W., and Dietrich, W.E., 2001, Hillslope evolution by nonlinear, slope-dependent transport: Steady state morphology and equilibrium adjustment timescales: Journal of Geophysical Research, v. 106, p. 16499, doi:10.1029/2001JB000323.

Roering, J.J., Perron, J.T., and Kirchner, J.W., 2007, Functional relationships between denudation and hillslope form and relief: Earth and Planetary Science Letters, v. 264, p. 245–258, doi:10.1016/j.epsl.2007.09.035.

Roering, J.J., Marshall, J., Booth, A.M., Mort, M., and Jin, Q., 2010, Evidence for biotic controls on topography and soil production: Earth and Planetary Science Letters, v. 298, p. 183–190, doi:10.1016/j.epsl.2010.07.040.

Lovell, J., 1969, Tyee Formation: Undeformed turbidites and their lateral equivalents: Mineralogy and paleogeography: Geological Society of America Bulletin, v. 80, p. 9–22, doi:10.1130/0016-7606(1969)80[2129:TFUTAT]2.0.CO;2.

Rosenqvist, I.T., 1970, Formation of vivianite in Holocene clay sediments: Lithos, v. 3, p. 327–334, doi:10.1016/0024-4937(70)90039-3.

Sadler, P.M., 1981, Sediment accumulation rates and the completeness of stratigraphic sections: The Journal of Geology, v. 89, p. 569–584, doi:10.1086/628623.

Sarna-Wojcicki, A.M., Champion, D.E., and Davis, J.O., 1983, Holocene volcanism in the conterminous United States and the role of silicic volcanic ash layers in correlation of latest-Pleistocene and Holocene deposits, *in* Wright, H.E., ed., Late Quaternary Environments of the United States, Volume 2: Minneapolis, Minnesota, University of Minnesota Press, p. 52–77.

Saunders, I., and Young, A., 1983, Rates of surface processes on slopes, slope retreat and denudation: Earth Surface Processes and Landforms, v. 8, p. 473–501, doi:10.1002/esp.3290080508.

Schaller, M., and Ehlers, T.A., 2006, Limits to quantifying climate driven changes in denudation rates with cosmogenic radionuclides: Earth and Planetary Science Letters, v. 248, p. 153–167, doi:10.1016/j.epsl.2006.05.027.

Schaller, M., von Blanckenburg, F., Veldkamp, A., Tebbens, L.A., Hovius, N., and Kubik, P.W., 2002, A 30 000 yr record of erosion rates from cosmogenic ^{10}Be in Middle European river terraces: Earth and Planetary Science Letters, v. 204, p. 307–320, doi:10.1016/S0012-821X(02)00951-2.

Scherler, D., Bookhagen, B., Wulf, H., Preusser, F., and Strecker, M.R., 2015, Increased late Pleistocene erosion rates during fluvial aggradation in the Garhwal Himalaya, northern India: Earth and Planetary Science Letters, v. 428, p. 255–266, doi:10.1016/j.epsl.2015.06.034.

Schumer, R., and Jerolmack, D.J., 2009, Real and apparent changes in sediment deposition rates through time: Journal of Geophysical Research, v. 114, p. F00A06, doi:10.1029/2009JF001266.

Schumer, R., Jerolmack, D., and McElroy, B., 2011, The stratigraphic filter and bias in measurement of geologic rates: Geophysical Research Letters, v. 38, p. L11405, doi:10.1029/2011GL047118.

Slim, M., Perron, J.T., Martel, S.J., and Singha, K., 2015, Topographic stress and rock fracture: A two-dimensional numerical model for arbitrary topography and preliminary comparison with borehole observations: Earth Surface Processes and Landforms, v. 40, p. 512–529, doi:10.1002/esp.3646.

Smith, D.J., 1992, Long-term rates of contemporary solifluction in the Canadian Rocky Mountains, *in* Dixon, J.C., and Abrahams, A.D., eds., Periglacial Geomorphology: Chichester, UK, Wiley, p. 203–221.

Snavely, P.D., Wagner, H.C., and MacLeod, N.S., 1964, Rhythmic-bedded eugeosynclinal deposits of the Tyee Formation: Oregon Coast Range: Kansas Geological Survey Bulletin 169, p. 461–480.

Stock, J.D., and Dietrich, W.E., 2006, Erosion of steepland valleys by debris flows: Geological Society of America Bulletin, v. 118, p. 1125–1148, doi:10.1130/B25902.1.

Sweeney, K.E., Roering, J.J., Almond, P., and Reckling, T., 2012, How steady are steady-state landscapes? Using visible-near-infrared soil spectroscopy to quantify erosional variability: Geology, v. 40, p. 807–810, doi:10.1130/G33167.1.

Tappeiner, J.C., Huffman, D.W., Marshall, D., Spies, T.A., and Bailey, J.D., 1997, Density, ages, and growth rates in old-growth and young-growth forests in coastal Oregon: Canadian Journal of Forest Research, v. 27, p. 638–648, doi:10.1139/x97-015.

Thompson, R.S., Anderson, K.H., Bartlein, P.J., and U.S. Geological Survey, 1999, Atlas of Relations Between Climatic Parameters and Distributions of Important Trees and Shrubs in North America: Conifers: U.S. Geological Survey Professional Paper 1650A, 269 p.

Tucker, G.E., and Slingerland, R., 1997, Drainage basin responses to climate change: Water Resources Research, v. 33, p. 2031–2047, doi:10.1029/97WR00409.

von Blanckenburg, F., 2005, The control mechanisms of erosion and weathering at basin scale from cosmogenic nuclides in river sediment: Earth and Planetary Science Letters, v. 237, p. 462–479, doi:10.1016/j.epsl.2005.06.030.

Walder, J., and Hallet, B., 1985, A theoretical model of the fracture of rock during freezing: Geological Society of America Bulletin, v. 96, p. 336–346, doi:10.1130/0016-7606(1985)96<336:ATMOTF>2.0.CO;2.

Wilkinson, M.T., and Humphreys, G.S., 2005, Exploring pedogenesis via nuclide-based soil production rates and OSL-based bioturbation rates: Australian Journal of Soil Research, v. 43, p. 767–779, doi:10.1071/SR04158.

Willenbring, J.K., and Jerolmack, D.J., 2015, The null hypothesis: Globally steady rates of erosion, weathering fluxes and shelf sediment accumulation during late Cenozoic mountain uplift and glaciation: Terra Nova, v. 28, p. 11–18, doi:10.1111/ter.12185.

Worley, I.A., and Jaques, D., 1973, Subalpine fir (*Abies lasiocarpa*) in coastal western North America: Northwest Science, v. 47, p. 265–273.

Worona, M.A., and Whitlock, C., 1995, Late Quaternary vegetation and climate history near Little Lake, central Coast Range, Oregon: Geological Society of America Bulletin, v. 107, p. 867–876, doi:10.1130/0016-7606(1995)107<0867:LQVACH>2.3.CO;2.

Zhang, P., Molnar, P., and Downs, W.R., 2001, Increased sedimentation rates and grain sizes 2–4 Myr ago due to the influence of climate change on erosion rates: Nature, v. 410, p. 891–897, doi:10.1038/35069099.

Science Editor: Aaron J. Cavosie
Associate Editor: Benjamin J.C. Laabs

Manuscript Received 6 February 2016
Revised Manuscript Received 29 August 2016
Manuscript Accepted 26 November 2016

Printed in the USA